universität wien

MASTERARBEIT

Titel der Masterarbeit

Mineralogical characterisation of a black smoker from the "Vienna woods" hydrothermal field, Manus Basin, Papua New Guinea: complex sulphide ores from a deep-sea hydrothermal system.

verfasst von

Simon Steger, BSc

angestrebter akademischer Grad

Master of Science (MSc)

Wien, 2015

Studienkennzahl lt. Studienblatt:	A 066 815
Studienrichtung lt. Studienblatt:	Masterstudium Erdwissenschaften
Betreut von:	Univ.-Prof. Dr. Lutz Nasdala

Acknowledgements

First of all, I thank Lutz Nasdala, who gave me the opportunity to work on this thesis and invested a lot of time supervising it. I am grateful to Christian L. Lengauer, Michael Götzinger, Christian Baal, Andreas Artač, Wolfgang Zirbs, Andreas Wagner and Max Svoboda for technical support. Constructive comments by Anton Beran, Wilfried Körner and Eugen Libowitzky are gratefully acknowledged. Xiasong Li is thanked for providing the NAA measurements. Special thanks go to my parents Claudia and Bernhard and my sister Katharina for supporting me in many different ways.

Declaration

I declare that this thesis was written by me and that it does not contains material, which has been submitted or accepted for an award of any other degree or diploma in any university or institution. All cited literature is listed without exception in the bibliography. To the best of my knowledge and belief this thesis contains no material previously published by any other person except where acknowledgment has been made.

Vienna, 2015

_____

Simon Steger

Abstract

This thesis summarises results of a MSc research that has addressed the examination and characterisation of the mineralogical relationships and chemical composition of a black smoker specimen origination from the "Vienna Woods" hydrothermal field. The specimen was sampled by Werner Tufar in 1990 during the OLGA II research cruise; it was donated by him to the mineral collection of the Institute of Mineralogy and Crystallography in 2013. Investigations on powders, polished sections and unprepared rock samples characterise the composition mineralogically in the most comprehensive way. A stepwise, pictorial documentation gives an excellent overview of mineral associations at different scales. Reflected light images show phase relationships and growth cycles between ore minerals such as pyrite, marcasite, sphalerite, wurtzite and chalcopyrite. By using detailed scanning electron microscopic (SEM)-studies, different phases and crystal forms of ores, gangue material and secondary minerals are discriminated. Moreover the bulk composition was measured by X-ray powder diffraction that confirmed pyrite, marcasite, sphalerite, wurtzite, chalcopyrite and galena as the most abundant sulphides. Sulphate minerals like gordaite, barite, anhydrite and gypsum occur as main phases in some samples. Raman spectroscopic measurements of both thick couples and unprepared rock samples were used to discriminate intergrowth of polymorphic minerals (e.g. pyrite and marcasite; FeS_2) and characterise different growth relationships of mineral associations. Rare sulphate minerals like jôkokuite, goslarite or metavoltine were detected by fingerprinting Raman spectroscopic measurements. Chemical analysis of major, minor and trace elements point out the heterogeneities of the different samples impressively. Special attention was paid on precious metals gold (up to 15 ppm) and silver (up to 518 ppm), due to their increased abundance. However no native gold inclusions are visible in reflected light. The applied mixture of both bulk and in-situ analysis in combination with detailed pictorial documentation shows the diversity of mineral assemblages and gives an impression of the strong geochemical heterogeneities in seafloor hydrothermal systems.

Zusammenfassung

Diese Arbeit untersucht und charakterisiert neben den mineralogischen Phasenbeziehungen auch die chemische Zusammensetzung eines „schwarzen Raucher“ Stückes vom Hydrothermalfeld „Wienerwald“. Das beprobte Exemplar wurde während der Forschungsreise „OLGA II“ von Werner Tufar 1990 geborgen. Im Rahmen seines goldenen Doktorates, stiftete Prof. Tufar das Stück dem Institut für Mineralogie und Kristallographie der Universität Wien. Messungen an Pulverproben, Erzschliffen und unpräparierten Gesteinsproben charakterisieren die mineralogische Zusammensetzung umfangreich. Anhand der bildlichen Dokumentation sind Mineralassoziationen bei unterschiedlichem Maßstab definierbar. Neben der Auflichtmikroskopie an polierten Erzschliffen wurden auch Aufnahmen von unpräparierten Proben am Rasterelektronenmikroskop durchgeführt. Außerdem konnten mittels Pulverdiffraktometrie die Hauptphasen identifiziert werden. Neben den häufigen Sulfiden (Pyrit, Markasit, Sphalerit, Wurtzit) treten auch Sulfate (Anhydrit, Gips, Baryt, Gordait) in erhöhten Mengen auf. Mit ortsaufgelösten, Raman spektroskopischen Messungen an Erzschliffen und unpräparierten Gesteinsproben sind polymorphe Minerale (z.B. Pyrit und Markasit; FeS_2) in-situ unterscheidbar. Außerdem können kleine Mineralaggregate gemessen werden. Seltene Minerale wie Jôkokuite, Goslarit und Metavoltin wurden durch Raman spektroskopische Messungen entdeckt. Die Bestimmung der Haupt-, Neben- und Spurenelemente zeigt eindrucksvoll die Heterogenitäten der unterschiedlichen Proben. Außerdem sind die Edelmetalle Silber (bis zu 518 ppm) und Gold (bis zu 15 ppm) in einigen Proben stark angereichert. Allerdings konnten keine gediegenen Goldeinschlüsse mittels Auflichtmikroskopie gefunden werden. Die angewandte Mischung aus Bulk- und in-situ Analysen, in Kombination mit einer detaillierten, bildlichen Dokumentation zeigt die Diversität der Mineralassoziationen und vermittelt den Eindruck von starken geochemischen Heterogenitäten in hydrothermalen Systemen am Ozeanboden.

Table of content

Acknowledgements iii
Declaration v
Abstract vii
Zusammenfassung ix
Table of content xi
1. Introduction 1
1.1 Formation of seafloor hydrothermal fluids through alteration of basaltic rocks 1
1.2 Formation of hydrothermal ore deposits 4
1.2 Manus Basin: geological setting 5
1.4 Hydrothermal field “Vienna Woods” 6
1.5 Objectives and rationale 7
2. Samples 9
2.1 Sample origin: from “Vienna Woods” to Vienna 9
2.2 Sample description 10
2.3 Sample preparation 12
3. Analytical methods 13
3.1 Imaging methods 13
3.2 X-ray powder diffraction 13
3.3 Raman spectroscopy 13
3.3 Chemical analysis 14
4. Results and discussion 16
4.1 Imaging methods 16
4.2 X-ray powder diffraction 20
4.3 Raman spectroscopy 22
4.3 Chemical analyses 28
4.5 Phase relationships and growth history 35
5. Conclusion 37
Appendix I: List of figures 39
Appendix II: List of tables 41
Appendix III: References 42
Appendix IV: Curriculum vitae 50

1. Introduction

1.1 Formation of seafloor hydrothermal fluids through alteration of basaltic rocks

At oceanic spreading centres submarine hydrothermal convection occurs if seawater enters a permeable medium (i.e. faulted and fissured crust) and heats up continuously. The hydrothermal fluid reaches temperatures exceeding 400 °C through heat sources like a magma chamber or a crystallising melt lens. As seawater penetrates downward and gets heated up consequently it undergoes chemical interactions with the surrounding rocks of the oceanic crust (Fig. 1; Alt 1995). Most hydrothermal vent systems are hosted in basaltic rocks (especially MORB like) and therefore the alteration products of basaltic rocks are well investigated by submersible observations and analyses of drill cores (Tivey 2007). Hydrothermal convection systems are divided into recharge, reaction and discharge zones with typical chemical reactions (Alt 1995).

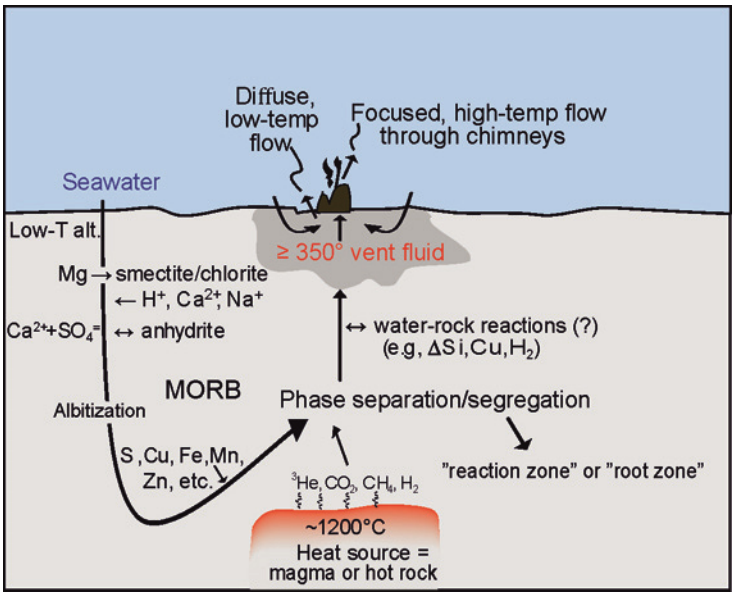

Fig. 1. Formation of vent fluids in mid-ocean-ridges (simplified sketch; modified after Tivey 2007).

The so called recharge zones are widespread areas, where seawater enters the crust, heats up and reacts as it penetrates downward. At low temperature (40–60 °C) seawater–basalt interaction results in oxidation of glass, olivine and plagioclase forming Fe-oxyhydroxides, ferric micas (e.g. celadonite), smectite (e.g. nontronite) and Mg rich smectite, thus alkali metals (K, Rb, Cs) as well as B are removed from the seawater through precipitation of nontronite and celadonite (Alt 1995). Meanwhile Si, S and sometimes Mg are added from the rock to the fluid (Tivey 2007). At elevated temperatures (above 150 °C) and

therefore in greater depth, seawater Mg is fixed by generation of Mg rich smectite and chlorite (Alt 1995). For example, Tivey (2007) explains chlorite precipitation as result of feldspar alteration: $4(NaSi)_{0,5}(CaAl)_{0,5}AlSi_2O_8 + 15Mg^{2+} + 24H_2O \Rightarrow 3Mg_5Al_2Si_3O_{10}(OH)_8 + SiO_2 + 2Na^+ + Ca^{2+} + 24H^+$.

Corresponding to the reaction equitation Na, Si, Ca and H^+ are added to the modified seawater, thus the fluid gets more acidic. Simultaneously alkali metals like Li, K, Rb and Cs as well as B are leached from the primary rocks (Alt 1995). These reactions partly compensate the uptake of alkalis and B during low temperature alteration. At 150–200 °C precipitation of anhydrite removes Ca and sulphate from the fluid and therefore inhibits the formation Ca-silicates (Bischoff and Seyfried 1978; Seyfried 1987). At higher temperatures (>250 °C) reduction of remaining seawater sulphate occurs as the fluid interacts with ferrous minerals like olivine, pyroxene and pyrrhotite (Shanks et al. 1981; Alt 1995; Tivey 2007). At elevated temperatures ion exchange reactions like the albitization of feldspar take place. The idealized reaction equation of Tivey (2007) shows that anorthite reacts with dissolved Na and SiO_2 to albite: $CaAl_2Si_2O_8 + 2Na^+ + 4SiO_2\ (aq) \Rightarrow 2NaAlSi_3O_8 + Ca^{2+}$.

The sum of reactions in the recharge zone is illustrated in Figure 1 and leads to a high temperature fluid that is slightly acidic, anoxic, alkali rich and Mg poor relative to the starting seawater. In the so called reaction zone fluid temperature increases rapidly from 200 °C to temperatures greater than 350 °C and chemical reactions like the leaching of metals (e.g. Zn, Cu, Fe, Mn) and S from the primary rocks occur (Fig. 1; Alt 1995). The breakdown of primary, magmatic sulphides and of ferromagnesian minerals in basalt adds Fe, Cu, Mn, Zn and S to the fluid (Hannington et al. 2005). The alteration of feldspar represents the main source for elements like Ba and Pb (Doe 1994). Due to the replacement of Fe-Ti oxides by titanite high Zn concentrations may be generated (Alt 1995). This leads to the alteration of the lower sheeted dikes and the upper gabbros of the oceanic crust at pressures of about 400 to 500 bars (Alt 1995; Tivey 2007). The fluid will separate into a vapour and volatile rich, low salinity phase and a Cl rich, brine phase, when the fluid crosses the two-phase curve at temperatures and pressures lower than the critical point for seawater [subcritical separation, i.e. boiling; (Von Damm 1995; Hannington et al. 2005; Tivey 2007)]. Most dissolved metals are transported at high temperatures as Cl-complexes and therefore they are mainly concentrated in the brine phase (Helgeson et al. 1981).

Finally the input of magmatic volatiles from the heat source modifies the fluid composition significantly (Fig. 1; Alt 1995). The amount of different volatiles depends strongly on the composition of the magma of the heat source. However the origin of these

components in the hydrothermal fluid is not always clear. For MOR vent fluids it is proven by isotopic analyses that magmatic CO_2 and ^3He are dissolved in the hydrothermal fluid (Alt 1995). Elevated CH_4 and H_2 concentrations may also originate from magmatic input. However other explanations like fluid-sediment interactions or possible biological sources may also be appropriate (Baross et al. 1982; Lilley et al. 1993; Kelley et al. 1993). At some back arc and arc systems input of SO_2 from crystallizing magma results in disproportionation of SO_2 forming sulphuric acid (Gamo et al. 1997). This reaction lowers the pH value of the hydrothermal fluid significantly. Furthermore some back arc and arc related magmatic fluids may also add metals (e.g. Fe, Cu, Zn, Ni) to the hydrothermal system which modify the fluid composition strongly (Scott and Yang 1996; Hannington et al. 2005). The PT conditions at the subsurface reaction zones are usually close to the critical point of water and therefore the physical properties of seawater change extremely: the density of the fluid decreases rapidly (down to 0.01 g/cm^3 at near-magmatic conditions), the coefficient of thermal expansion (α_f) and the heat capacity (C_p) reach maxima, whereas the viscosity reaches a minimum at 225 °C (Norton 1984). "These properties combine to limit further heating of the fluid, provide maximum buoyancy forces, and cause rapid up flow of hydrothermal fluids" (Alt 1995). Estimated subsurface flow rates are in the order of 0.7–5 m s^{-1} (Macdonald et al. 1980; Converse et al. 1984; Ginster et al. 1994) and 0.5–1 m s^{-1} (Delaney et al., 1987). However the fluid does not attain equilibrium during ascent. Due to the rapid pressure decrease, quartz becomes saturated, but cannot precipitate because of kinetic barriers (Tivey 2007). Chemical conditions (pH, temperature, O_2 content etc.) change abruptly when the fluid exits the seafloor and suddenly many minerals become saturated and precipitate.

Different volcanic and tectonic settings of seafloor hydrothermal systems affect the vent fluid composition strongly. Hydrothermal fluids from MORB hosted systems show a significantly different chemical signature as in ultramafic-dominated host rocks, sedimented environments or in arc and back-arc settings (Hannington et al. 2005). Another important factor regarding vent fluid composition is the source of heat that drives hydrothermal convection, because the generated fluid temperature affects directly the mineral-water reactions (Tivey 2007). Temperature, pH value, chlorinity and redox conditions are the main factors affecting the metal concentration in hydrothermal fluids (Seyfried and Ding 1995; Seyfried et al. 1999). Hannington et al. (2005) number the average metal concentration in vent fluids with ~300 ppm ($\triangleq$300 mg/l), however extreme values of less than 10 ppm in vapour-phase fluids and more than 1300 ppm in some brines are also observed.

1.2 Formation of hydrothermal ore deposits

Hydrothermal venting systems are roughly divided into focused "black smoker", "white smoker" and diffuse fluid systems, regarding their colour impression and fluid flow rate. The colour of the "smoke" depends on the dominant mineral species which precipitates [i.e. either sulphide dominated (dark colour) or sulphate and SiO_2 dominated (white colour)]. High temperature, sulphide dominated, focused "black smoker" fluids attain venting temperatures up to ~400 °C, whereas lower temperature, barite and SiO_2 dominated, focused "white smoker" fluids vent at temperatures of ~250–280 °C. Diffuse low temperature fluids (~100 °C) also occur, when the fluid cools down before venting (Corliss et al. 1979; Edmond et al. 1979; Spiess et al. 1980).

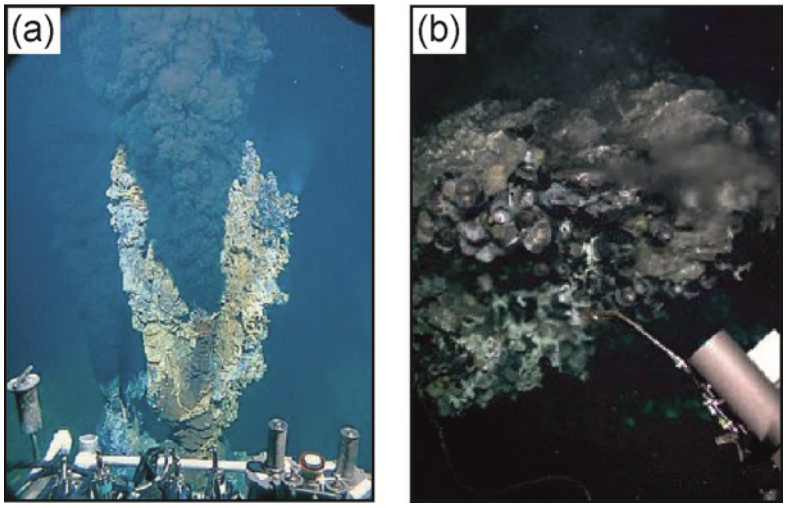

Fig. 2. Photograph of an active black smoker chimney in the southern part of the East Pacific Rise, taken from the submersible Alvin (**a**). Photograph of a diffuse venting spire in the "Vienna Woods" vent field, Manus basin (**b**). Both images modified after Tivey (2007).

These fluids build up typical hydrothermal deposit structures such as sulphide rich chimneys and metalliferous sediments (Haymon and Kastner 1981). Growth models for black-smoker chimneys are given by Haymon (1983) and Goldfarb et al. (1983). During initial growth, anhydrite and trace amounts of sulphides precipitate with growth rates up to 30 cm/day (Goldfarb et al. 1983). The highly permeable, anhydrite-rich layer is bounded on either side by fluids of different compositions and temperatures and provides a substrate where further minerals grow. Continued mixing between seawater and hydrothermal fluid lowers the porosity of the chimney wall by precipitation of sulphates and sulphides and isolates the hot hydrothermal fluid inside. As mixing is inhibited, a chalcopyrite-rich layer precipitates along the inner side of the open conduit. Advection and diffusion of seawater and

hydrothermal fluid across the wall results in precipitation of minerals within pore space of the wall (Tivey and McDuff 1990; Tivey 1995).

However lower-temperature (<300 °C) fluids often show different morphologies and compositions compared to their high temperature counterparts. Slower fluid flow rates and lower buoyancy lead to the formation of more porous, bulbous chimneys (Koski et al. 1994). Moreover mineral textures show that fluid flows through several micro channels. In general, these chimneys are enriched in Zn sulphides with fewer amounts of Cu-Fe sulphides (Haymon and Kastner 1981; Koski et al. 1994).

At larger scale, subsurface mixing of seawater with hydrothermal fluid results in precipitation of enormous amounts of anhydrite, pyrite and chalcopyrite at the TAG active mound (26 °N, mid-atlantic ridge) (Tivey et al. 1995). The morphology, composition and mineral zonation are similar to those observed in Cyprus-type ore bodies and therefore the processes responsible for the formation of these two deposits may be similar too (Constantinou and Govett 1973; Humphris et al. 1995; Tivey et al. 1995).

The lifetime and size of hydrothermal venting areas are directly coupled to the spreading rates: at fast spreading centres hydrothermal fluids circulate at relatively shallow depths (1–2 km); due to the shallow, subaxial magma, hydrothermal discharge lasts only 10 to 100 years (Hannington et al. 2005). Intermediate and slow-spreading centres enable deep fluid circulation (5–8 km) which results in large deposits and periods of hydrothermal activity lasting 10^3–10^5 years (German and Parson 1998; Hannington et al. 2005).

1.2 Manus Basin: geological setting

The Manus back-arc basin in the Bismarck Sea, Papua New Guinea shows a rapid divergent rate of about 100 mm/year which is ascribed to the subduction of the Solomon microplate beneath the South Britain microplate (Taylor 1979; Davies et al. 1987; Martinez and Taylor 1996; Binns et al. 2007). The crust of the Manus Basin is trapped in the stress zone of the Pacific plate and the Australian plate. This leads to an additional clockwise rotation (Tufar 1992) and a very complex structure of the spreading zone. The Manus Spreading Center (MSC) is bordered by the Willaumez and Djaul transform faults (Martinez and Taylor 1996). Mainly basaltic lavas erupt there (Both et al. 1986; Sinton et al. 2003) and "[…] the bottom is everywhere covered with pillow lava" (Lisitsyn et al. 1993). The eastern Manus Basin is located between the Djual and Weitin transform faults (Fig. 3) and "volcanism associated with the incipient rifting of pre-existing intermediate/felsic crust has produced a complex series of en echelon neovolcanic ridges […] and volcanic domes on the seafloor known as the

Eastern Manus Volcanic Zone" (Reeves et al. 2011). The composition of lavas from these ridges shows andesitic or rhyolitic characteristics (Sinton et al. 2003). There are several hydrothermal active localities in the East Manus Basin such as the PACMANUS (Papua New Guinea–Australia–Canada–MANUS) system as well as the DESMOS and SuSu Knolls system (Fig. 3).

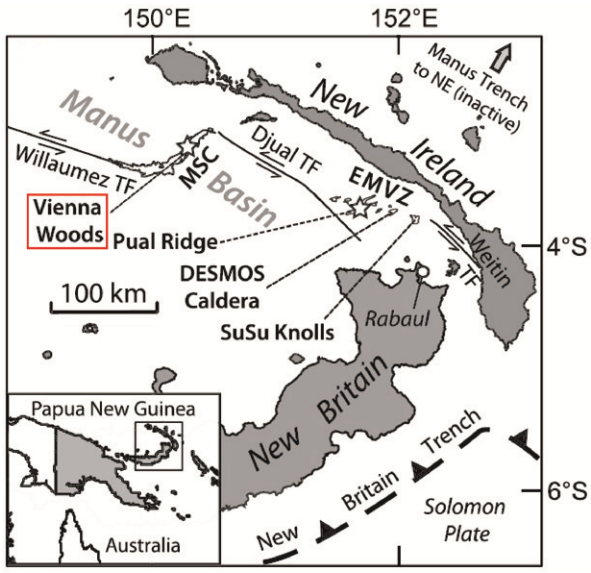

Fig. 3. Simplified map showing the location of the hydrothermal field "Vienna Woods" in the Manus Basin (modified after Reeves et al. 2011).

1.4 Hydrothermal field "Vienna Woods"

The unsedimented Vienna Woods field (3° 9,86' S, 150° 16,78' E) "[…] is confined to a 2-km wide axial volcanic swell in the rift valley of the spreading centre […]" (Lisitsyn et al. 1993). It is hosted in MORB-like basalt; however lavas evolve along MSC to more intermediate composition (Shaw et al. 2004; Reeves et al. 2011). Recent hydrothermal activity extends over an area of about 150 by 100 m at ~2500 m water depth (Tufar 1990b; Tivey et al. 2007). Black and grey fluids are venting at 273–302 °C with a measured pH (25 °C) value of 4.2–4.7 with a constant endmember fluid composition; however the venting temperature has been decreasing slightly since the last 20 years (Lisitsyn et al. 1993; Auzende et al. 1996; Gamo et al. 1997; Douville et al. 1999; Fourre et al. 2006; Tivey et al. 2007; Reeves et al. 2011). Both active and inactive sluphidic chimneys occur "[…] at a density of some 5-8 tubes per 10 m^2" (Lisitsyn et al. 1993).

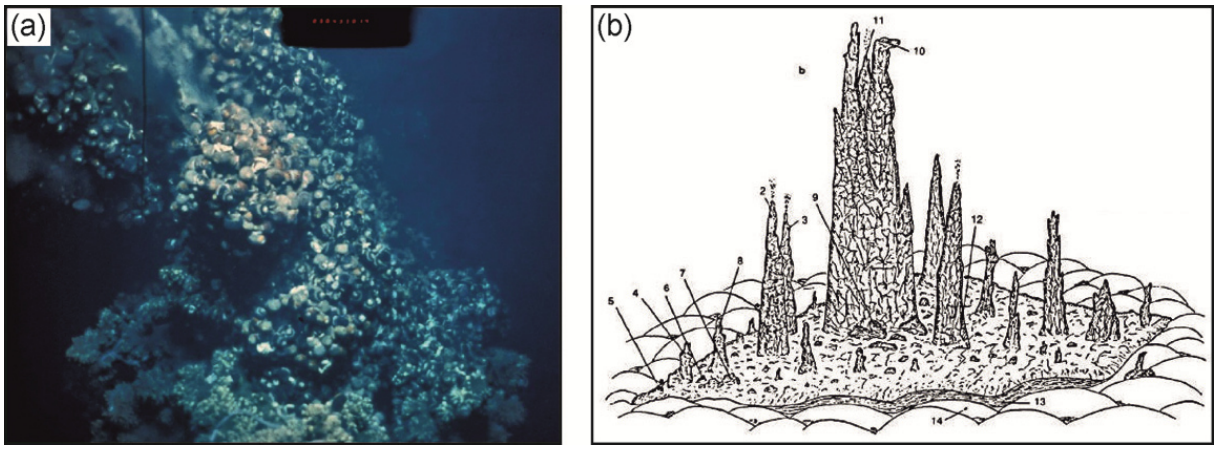

Fig. 4. Impressions from the hydrothermal field "Vienna Woods". (**a**) Photograph taken from the submersible *Mir 1* showing an active chimney which is covered by snails (*Olgaconcha Tufari* and *Alviniconcha cf. hessleri*), barnacles (*eochionelasmus ohtai*), sea cucumbers (*Chiridota hydrothermica*) and crabs (*Munidopsis cf. marianica*) (image courtesy of Werner Tufar). (**b**) Schematic drawing of chimneys in the "Vienna Woods" field (modified after Lisitsyn et al. 1993).

1.5 Objectives and rationale

This MSc thesis examines and characterises the mineralogical relationships and chemical composition of a "black smoker" fragment, taken from an active chimney. A stepwise, pictorial documentation gives an excellent overview of mineral associations at different scales. Beside phase analyses of powder samples, space resolved analyses of both thick couples and unprepared rock samples are used to characterise gangue material, secondary minerals and sulphide ores properly. By using Raman spectroscopic analyses different growth cycles of mineral associations are discriminated. Chemical analyses of major, minor and trace elements point out the heterogeneities of the different samples impressively. Special attention was paid on precious metals Au and Ag, due to their increased abundance. The over-arching objectives of this thesis are:

(1) to find and characterise different mineral associations with an effective mixture of analyses methods;
(2) to give an detailed pictorial documentation of both unprepared rock samples and polished sections;
(3) to correlate the temperature with different mineral associations;
(4) to define the growth history of different mineral associations;
(5) to correlate trace elements with different mineral associations.

In the last decades the main focus of research laid on the determination of element abundances in the hydrothermal vent fluids. Precise measurements of trace elements have always been important for geochemical information of sub seafloor processes. Especially

REE (rare earth elements) patterns of hydrothermal fluids have been of recent interest (Klinkhammer et al. 1994; Mitra et al. 1994; Bau and Dulski 1999; Douville et al. 1999; Carddock et al. 2010).

Only few studies deal with detailed mineralogical characterisation of sulphide chimneys in the Manus basin. Shadlun et al. (1993) give a first description and pictorial documentation by reflected light microscopy of sulphide ores from the hydrothermal field "Vienna Woods". They distinguish between different mineral associations and growth stages of ore minerals. Moreover chemical investigations by microprobe analyses characterise different minerals and mineral associations in terms of major and minor element composition (Shadlun et al. 1993). Moss and Scott (2001) investigated the mineralogy of gold rich sulphides deposits in the eastern Manus basin. They found native gold inclusions up to 5 µm in tennantite and chalcopyrite. Carddock (2009) describes the mineralogy of sulphide chimneys at different venting fields in the Manus basin. He compares element abundances of rock samples from open conduit chimneys, diffuser type edifices and relic spires of different localities. Raman spectroscopic studies on hydrothermal ore systems have been reported recently by White (2008) and Breier et al. (2010). During the last years, sea-going Raman systems have been built to analyse in-situ minerals, fluids and organic compounds (Battaglia et al. 2004; Brewer et al. 2004; Schmidt et al 2004; White et al. 2006). This research puts a focus on micro-Raman spectroscopy and points out the challenges and advantages of this method for sulphide rich ore samples.

This MSc-thesis represents an attempt to characterise sulphide rich "black smoker" samples mineralogically in the most comprehensive way. The applied mixture of both bulk and in-situ analyses in combination with detailed pictorial documentation shows the diversity of mineral assemblages and gives an impression of the strong heterogeneities in seafloor hydrothermal systems.

2. Samples

2.1 Sample origin: from “Vienna Woods” to Vienna

From April 29 to June 25, 1990 the research cruise "SONNE 68 – OLGA II" (Ozeanische Lagerstatten: Geologisch-Mineralogische Analyse = Oceanic Deposits: Geological-Mineralogical Analysis) of the University of Marburg, directed by Prof. Werner Tufar, was the first to conduct a detailed economic-geological mapping of coherent deposits of recent hydrothermal mineralisation in a back-arc basin with detailed statistical sampling (Tufar 1990a). At the first successful research cruise OLGA I Prof. Tufar went to the East Pacific Rise, afterwards he organised the international research project OLGA II to prove recent hydrothermal activity in the Manus basin, Papua New Guinea.

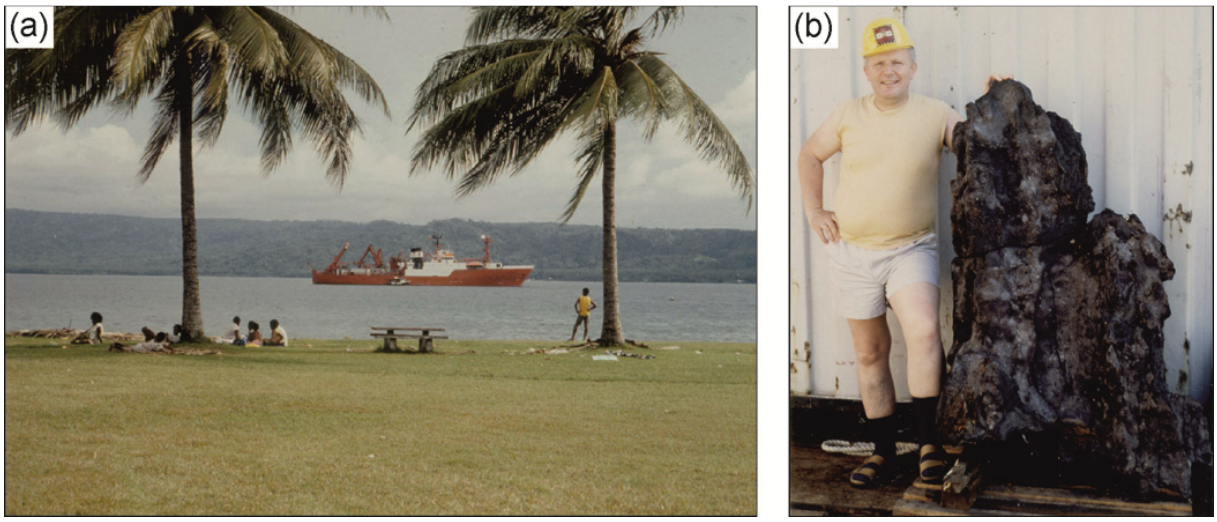

Fig. 5. Impressions from the 1990 research cruise OLGA II. (**a**) Research vessel “Sonne” in the port of Rabaul, New Britain (modified after Tufar 1991). (**b**) May 12, 1990: Werner Tufar on board of “Sonne”, with a fragment of a just recovered, black smoker chimney, weighing ca. 1500 kilograms (image courtesy of Prof. Tufar).

First evidence of hydrothermal activity in this area was described by Both et al. (1986). Detailed mapping of the Manus Spreading Center by SeaBeam profiling, OFOS (Ocean Floor Observation System) surveys, as well as by TV Grab studies revealed a number of active hydrothermal areas associated with recent hydrothermal mineralization (Tufar 1990a). In June 1990 the USSR Academy of Sciences "Akademik Mstislav Keldysh" 21st Research Cruise, directed by Prof. Lisitsyn was simultaneously conducted in this region and a spontaneous cooperation was established. The detailed maps of the OLGA II program offered an excellent basis for the Russian submersible dives and as reward for the helpful results Prof. Werner Tufar could join a dive.

The results of the research cruise OLGA II include the discovery and sampling of four new hydrothermal fields as well as the first description of new species (Fig. 4).The largest and most active area was named “Vienna Woods” (Tufar 1990b), “[…] because of the abundance of narrow chimneys resembling tree trunks” (Lisitsyn et al. 1993). On the occasion of his golden doctorate diploma, Prof. Tufar donated a black smoker fragment, taken from an active chimney (email conv. W. Tufar 10. 02. 2014), to the mineral collection of the Institute of Mineralogy and Crystallography, University of Vienna.

2.2 Sample description

The specimen is a cask-shaped segment of an active sulphide chimney 57 cm in length, 40 cm in width and 30 cm in height (maximum values). The segment shows a layering in terms of colour, whereas the outermost light, brownish zone of alteration (Fig. 6) points out the rock-seawater interaction. A whitish zone in the outer region is dominated by sulphates and SiO_2. The main body of the specimen is composed of a fine grained, porous and whitish grey to dark grey mass. Narrow conduits and cavities are oriented parallel to the longitudinal axis of the chimney. Nests of well-shaped crystals occur in the fine grained matrix and on the walls of the open tunnel ways. Spots of greyish-yellow areas and dense, whitish-grey zones (Fig.6 BS2) are also observed.

Seven representative samples (Fig. 6) at morphological different points were taken. The first sample (BS1) represents the oxidized exterior of the chimney. The polished section of this sample was prepared as a cross section of the outermost, brownish area to distinguish the change of phases in this zone. The area at pin BS2 is a dense, whitish-grey zone which overlays the typical matrix material. Sample BS3 was taken from an open conduit wall with well-shaped and large crystal aggregates (Fig.6d). Pin BS4 represents the sampling site of a greyish-yellow, very fine grained and porous zone in the middle of the specimen. It was a great challenge to get a polishable piece of rock from this area. Sample BS5 was taken from a nest of crystals (Fig.6e) and the polished section was prepared as a cross section to identify the transition from the crystal rich zone to the matrix material. Finally samples BS6 and BS7 represent the matrix material at two different areas.

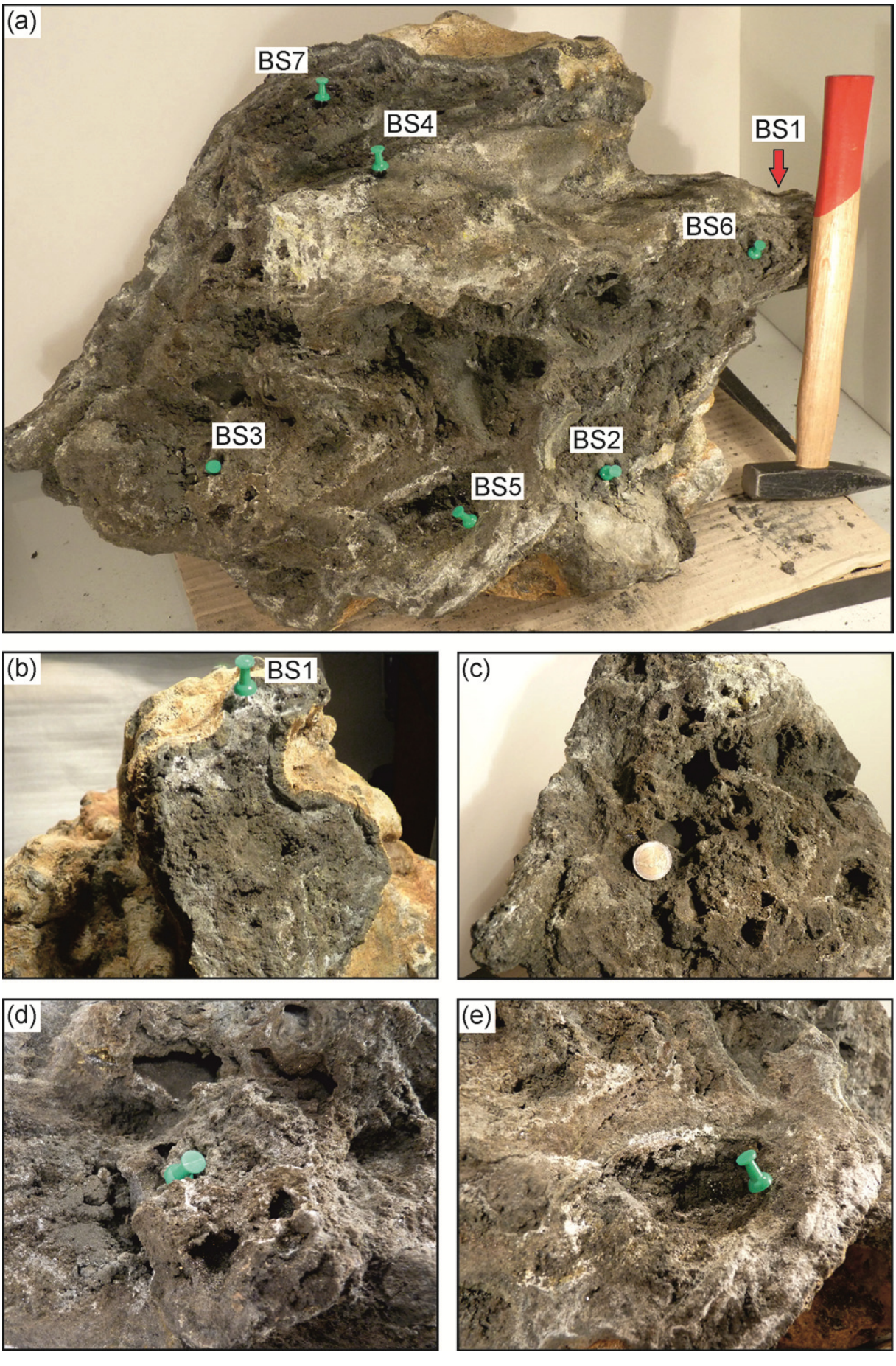
(a)
BS7
BS4
BS1
BS6
BS3
BS2
BS5
(b)
BS1
(c)
(d)
(e)

Fig. 6. Photographs of the black smoker sample. Small green pins mark the sampling sites (cf. labels). (**a**) View onto the base (i.e. along the former venting direction). The position of BS1 at the top of the specimen cannot be seen directly; it is indicated by a black arrow. (**b**) View at the top side. Note that the surface of the black smoker, which was in direct contact with cold seawater, shows alteration indicated by light, brownish colours. (**c**) View at the bottom which shows fairly large conduits (black holes). (**d**) Open conduit wall at the bottom of the black-smoker specimen (sampling site BS3). (**e**) A nest of well-shaped crystals within the porous, fine grained matrix (sampling site BS5).

2.3 Sample preparation

The different analyse techniques require unprepared rock samples, polished sections and powders. Therefore an average sample amount of ~4 g was necessary. Powdered samples were provided for X-ray powder diffraction, ICP-OES, ICP-MS and neutron-activation analyses. Polished sections were prepared for reflected light microscopy and Raman spectroscopy. Finally, unprepared rock samples were used for the detection of SEM-images and for Raman spectroscopy.

3. Analytical methods

3.1 Imaging methods

Unprepared rock samples and polished sections were used for pictorial documentation to get both, detailed photographs of 2D textures and 3D images of typical crystal aggregates. Optical investigations of polished sections are the easiest way to get an overview of the ore associations in the different samples. Special growth textures and phase relationships are also visible in the reflected light. However gangue material cannot be identified properly. An optical microscope Olympus BX51 equipped with an Olympus DP70 digital camera system was used.

Secondary electron images of the unprepared rock samples were obtained by means of a FEI Inspect S50 scanning electron microscope equipped with a tungsten cathode at12.5 kV, using a spot size of 5 and a working distance of 9.2 mm. The samples were not coated and therefore, to prevent the accumulation of electrostatic charge at the surface, samples BS1, BS2, BS3, BS4 and BS7 were measured in the low vacuum mode. The samples BS5 and BS6 are enough electrically conductive thus the high vacuum mode was appropriate.

3.2 X-ray powder diffraction

X-ray powder diffraction offers the opportunity to analyse different minerals of a phase mixture simultaneously. Small sample preparation and the discrimination between polymorphic phases are the main advantages of this method. However strong absorption, and the fact that only the most abundant phases could be detected, are the main disadvantages. Moreover analyses of powder lead to the loss of space resolved information.

X-ray powder diffraction data of the seven samples were obtained by means of a Philips X'Pert powder X-ray diffractometer using CuKα radiation. A spatula tip of powder was prepared on a Si sample holder for low background interferences. The measured range was 5–75° 2θ.

3.3 Raman spectroscopy

Raman spectroscopy provides the unique opportunity to analyse non-destructively polished sections as well as unprepared rock samples. Only minute amounts of sample, on the order of a few cubic micrometres, are needed for the detection of fingerprint spectra. Thus gangue material, secondary minerals and sulphide ores are identified properly. Point analyses on

single crystals and mineral aggregates determine minerals, which are to less abundant for powder X-ray powder diffraction. Furthermore polymorphic minerals like pyrite and marcasite can be discriminated. However there are also disadvantages: some minerals like galena or halite do not have Raman active vibrations and therefore they cannot be identified by Raman spectroscopy. Raman active sulphide minerals are weak Raman scatterer, and that implies poor peak/background ratios, broad bands, and strong absorption of the laser light. Therefore a filter has to be interconnected to avoid sample alteration and this increases the acquisition time significantly. Another problem is the availability of reliable reference spectra for natural sulphide minerals.

Measurements were performed on a Horiba Jobin Yvon Lab Ram HR Evolution spectrometer and a Horiba Jobin Yvon LabRAM-HR 800 spectrometer, both equipped with an Olympus BX41 microscope and a CCD detector. All samples were excited with a 532 nm (pyrite, marcasite, chalcopyrite) or a 633 nm (sphalerite, wurtzite, sulphur, sulphates) laser through a 50× long-distance objective (0.55 nA). The holographic grating was set on 1800 grooves/mm and the confocal hole was opened to 1000 µm. Especially sulphide minerals absorb the incident laser light strongly and therefore, to avoid sample alteration, a 50 % or sometimes a 25 % filter must be interconnected, so that the acquisition time increases up to 100 seconds (wurtzite). The acquisition time for non-sulphide minerals ranges between 2 (sulphur), 5 (e.g. gypsum) up to 20 (e.g. metavoltine) seconds.

The band position and full width at half maximum (FWHM) were calculated using the PeakFIT® software. After an appropriate background correction, combined Gaussian-Lorentzian band shapes were assumed in the fit procedure. For the band position an error of ±0.5 cm^{-1} is assumed.

3.3 Chemical analyses

For the chemical characterisation of the samples some difficulties must be overcome. The extraordinary sample composition with SiO_2, sulphides and sulphates (mainly barite and calcium sulphates) as main phases make the choice of digestion routines difficult. Barite and anhydrite are hardly soluble in conventional acidic digestion routines, but sulphidic sulphur outgases under high temperature conditions. Therefore fusion bead and microwave digestion routines cannot be applied successfully and danger of explosion may occur. These challenges can only be solved in laboratories which have routine analyses for complex sulphide ores. So I decided to send the samples to Activation Laboratories Ltd., Ontario, Canada to determine

major, minor and trace elements. The extraordinary composition of major elements busts the detection limits of the ICP-MS analyses. Therefore, to get confidential results, a modified ICP-OES measurement was chosen: in addition to the typical major and minor elements Al, Ca, Fe, K, Mg, P, S and Si, four unusual elements (Ba, Cu, Pb, Zn) were also treated like major ones. There was no opportunity to get trustful results for sulphur, because during the digestion routines for the ICP-MS and ICP-OES analyses sulphur may outgas easily. A CHNS analysis with an ELEMENTAR vario MACRO analyser also failed because "only 50–70% of the $BaSO_4$ breaks up in the flame" (pers. comm W. Körner) and the error cannot be calculated.

For the determination of the precious metals silver and gold a neutron activation analysis (NAA) was chosen. This is the most sensitive method for gold and it offers very low detection limits. Neutron activation analyses were carried out by Xiasong Li at ZTWB Radiochemie München, Technische Universität München, Germany. All powdered samples were packed in polyethylene foil, irradiated with neutrons (ϕ_{th} ~3.6×10^{13}/cm^2s) for 30 (BS1–BS4) or 15 minutes (BS5–BS7) and measured on HPGe detectors. The determination of element concentrations was performed, using the k_0 method. For quality control several elements (e.g. Ba, Cu, Fe, Mo, Co) were measured simultaneously with silver and gold.

4. Results and discussion

4.1 Imaging methods

Reflected-light optical microscopy is a most suitable technique for the study of opaque poorly transparent ore minerals of hydrothermal origin, including pyrite (FeS_2), marcasite (FeS_2), wurtzite (ZnS), sphalerite (ZnS), chalcopyrite ($CuFeS_2$), and galena (PbS). Pyrite (reflectance 51.7 %) and marcasite (48–55.8 %) show a typical yellowish, white colour (Spry and Gedlinske 1987). The ZnS polymorphs sphalerite (16.7 %) and wurtzite (17.2–19.5 %) are characterised by low reflectance and hence dark grey colours are observed (Spry and Gedlinske 1987). Note, however, that both the two FeS_2 polymorphs, and sphalerite and wurtzite, are often closely inter-grown with each other. Therefore, Pyrite–marcasite and sphalerite-wurtzite, respectively, often cannot be readily distinguished by reflected-light optical microscopy. Under reflected light chalcopyrite (44.6–45 %) reveals a characteristic yellow to brassy yellow colour whereas galena (43.1 %) shows a typical white to light grey colour (Spry and Gedlinske 1987). Chalcopyrite and galena therefore can be discriminated easily on the basis of their colour.

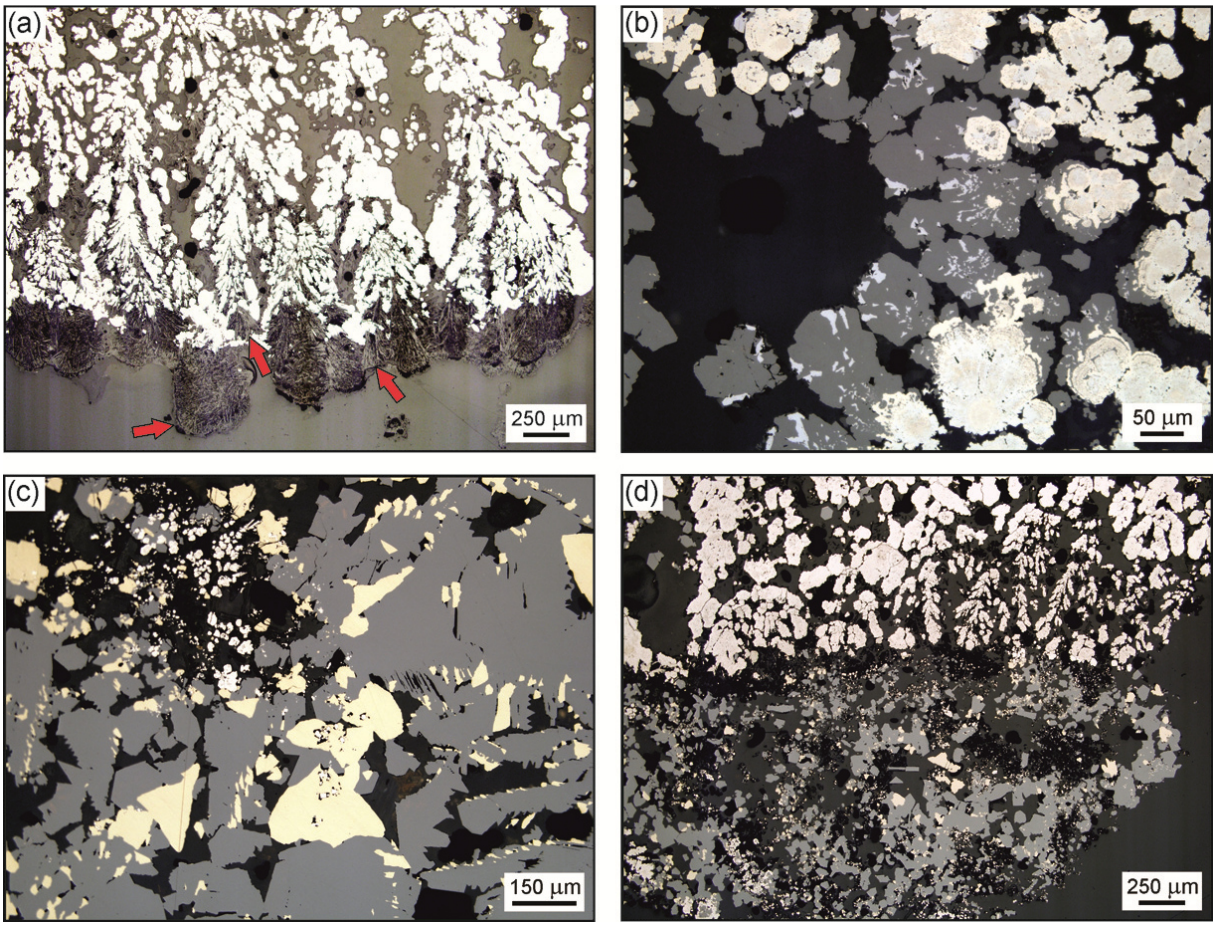

Fig. 7. Reflected-light photomicrographs of common mineral associations. (**a**) Cross section of the outermost, light brownish zone (BS1): dendrites of pyrite-marcasite (light yellow) in a matrix of amorphous SiO_2 and barite (red arrows) rich nodules (dark grey, black rounded areas, compare Fig. 10a). (**b**) Intergrowth of galena (light grey), sphalerite (dark grey) and pyrite (light yellow). (**c**) Chalcopyrite (yellow) inter-grown with ZnS (grey) and minor pyrite (light yellow), indicating elevated formation temperatures. (**d**) Transition zone of different mineral associations: a zone dominated by dendrites of FeS_2 (light yellow) adjoins a zone rich in ZnS (dark grey) and chalcopyrite (yellow). Round, black areas are empty pores in the sample.

Pyrite and minor marcasite show dendritic or collophorm growth textures (Fig. 7). The bulk of pyrite and marcasite was deposited together with an early generation of sphalerite with wurtzite and minor chalcopyrite. Collophorm pyrite grains are sometimes corroded and show surficial, thin layers of ZnS (Fig. 7b). The Zn sulphides occur as coarse grained (~1 mm), tabular aggregates, whereas wurtzite is commonly observed in the form of hexagonal cross sections. In sample BS1 (outermost, brownish zone), sphalerite and galena interfinger one with another. This indicates that the deposition of these two minerals was frequently overlapping (Fig. 7b). This association corroded and overgrew the early pyrite and marcasite crystals. Furthermore, dendritic, saw-blade-like growth of mainly wurtzite with fine grained, euhedral chalcopyrite inclusions was also observed (Fig. 8b). Shadlun et al. (1993) concluded that the chalcopyrite inclusions grew epitaxially on the ZnS grains and crystallized together with the ZnS dendrites. These tiny, well-shaped chalcopyrite crystals represent a late generation of chalcopyrite. The early generation shows larger, subhedral grains (up to 300 µm), which are located interstitial between ZnS aggregates (Fig. 7c). They are partly corroded and have overgrown pyrite crystals. This suggests that chalcopyrite must have formed later than pyrite. However, chalcopyrite coatings on ZnS crystals are common, which implies that nearly simultaneous formation with ZnS is likely.

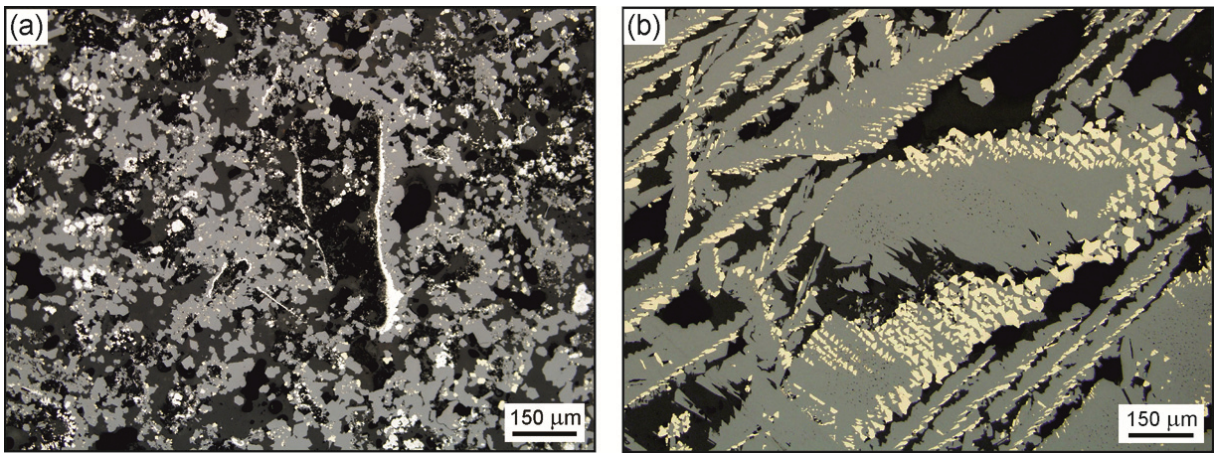

Fig. 8. Reflected-light photomicrographs of rare mineral associations. (**a**) Elongated borehole representing a biogenic trace (BS7). (**b**) Oriented inter-growth of dendritic ZnS (grey) with a multitude of fine-grained, idiomorphic chalcopyrite crystals (yellow; BS3).

All samples yield remarkable growth textures that appear most useful in terms of the minerogenetic interpretation. Sample BS1, prepared as cross section of the outermost, light brownish zone (which was in direct contact with the seawater), is composed of bulbous aggregates of acicular barite and dendritic FeS_2 (Fig. 7a). Typical lath-shaped crystals and radiating clusters of barite have replaced and corroded the FeS_2-crystals. This observation suggests that the deposition of barite must have occurred at a later stage.

Really exciting observation were made in the transition zone of two obviously different mineral associations (Fig. 7d). Here, a FeS_2-rich zone adjoins a zone dominated by ZnS and chalcopyrite, accompanied by a network of empty holes. Dendritic pyrite and marcasite and small amounts of early sphalerite and wurtzite represent an early growth stage. Because unfilled holes are present, it appears most likely that the sphalerite–wurtzite–chalcopyrite association has formed in an open, hot conduit. Relictic biogenic burrows, which are remineralized by pyrite, are typical of the matrix material (Fig. 8a).

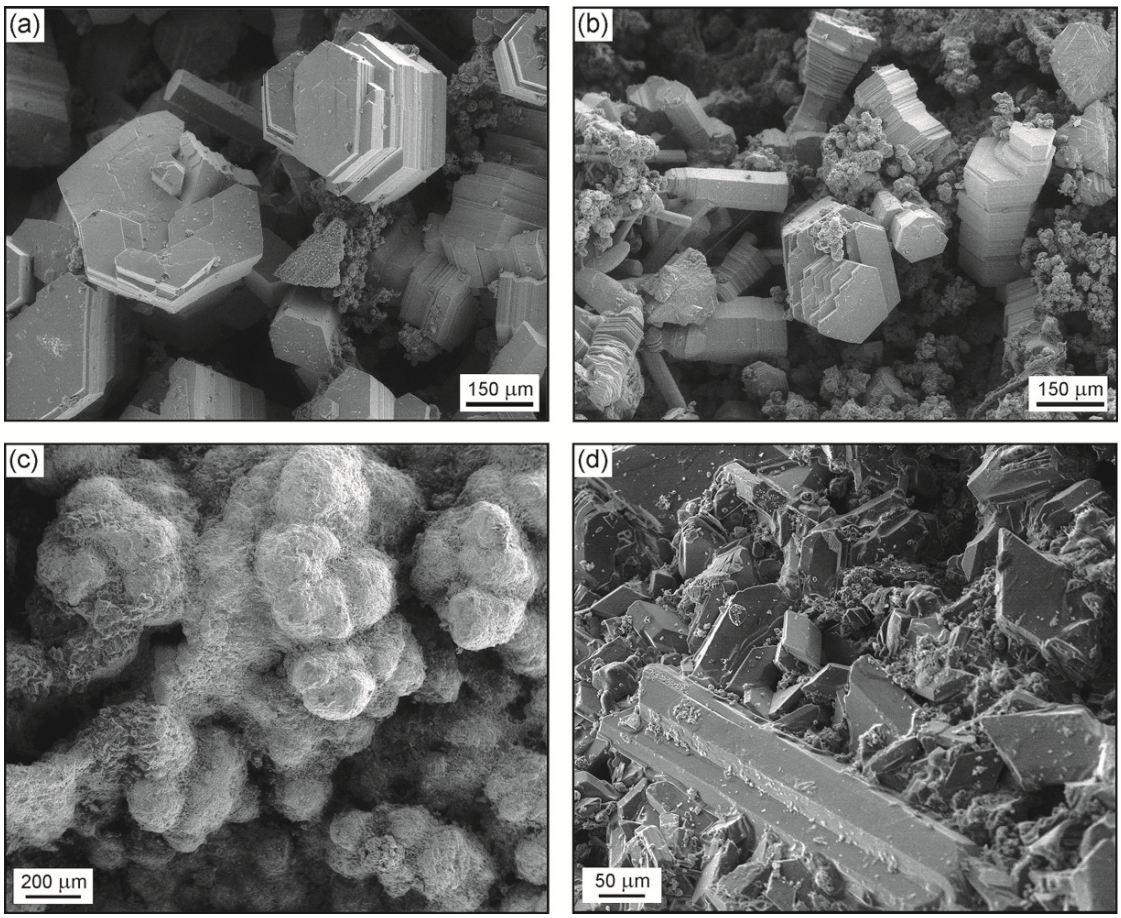

Fig. 9. Secondary electrons images of typical mineral associations. (**a**) And (**b**) ZnS crystals (piled pseudohexagonal grains, columnar crystals) in a matrix of fine grained barite and amorphous silica (BS7). (**c**) Barite-rich nodules (surface of BS1; compare Fig. 8a). (**d**) Lath-shaped and rhomboidal gypsum and anhydrite crystals (BS2).

Detailed SEM studies reveal different crystal forms and phase relationships for both the ore minerals and the gangue material. Piled, well-shaped ZnS crystals associated with tube-like aggregates of fine-grained pyrite, amorphous silica and chalcopyrite are commonly observed (Fig 9a and b). Sample BS2, taken from the whitish, grey zone, mainly contains lath-shaped and rhomboidal crystals of gypsum and anhydrite (Fig. 9d). Because anhydrite precipitates at temperatures above 150 °C, and forms secondary gypsum upon hydration at lower temperatures, the detection of anhydrite and gypsum indicates intense seawater – fluid mixing. The SEM images obtained in the outermost zone (sample BS1) show barite-rich nodules (Fig. 9c) with an abraded surface, which is most likely, the result of bioerosion.

Between the abraded barite nodules, holes with well-shaped ZnS crystals appear. These ZnS crystals are partly overgrown and corroded by small globules of amorphous silica (Fig. 10) and rounded sulphur crystals. In-situ energy dispersive X-ray analysis (EDX) yields the presence of silicon, zinc and sulphur. Such overgrowth and corrosion of the ZnS surface was only observed in sample BS1.

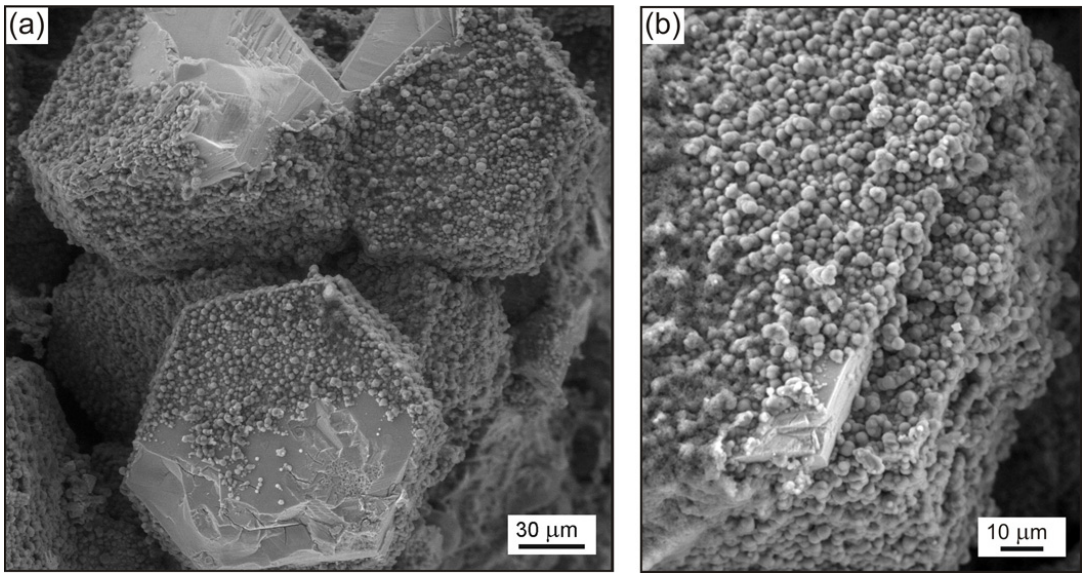

Fig. 10. (**a**) And (**b**) Secondary electrons images of tabular ZnS crystals overgrown by amorphous silica spherules (BS1).

Moreover pictorial documentation by scanning electron microscopy gave the first hint for the presence of gordaite ($Zn_4Na(OH)_6(SO_4)Cl \cdot 6H_2O$). Thin, ribbon-like crystals, stacked to aggregates are associated with primary ore minerals (Fig. 11). In-situ energy dispersive X-ray analysis (EDX) yields the presence of Na, Zn, S and Cl.

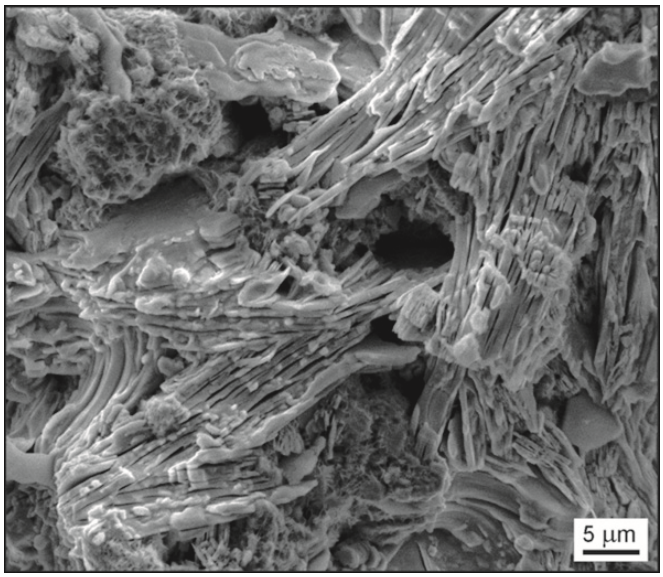

Fig. 11. Secondary electrons image of gordaite layers (sample BS5).

4.2 X-ray powder diffraction

X-ray powder diffraction offers the opportunity to analyse different minerals of a phase mixture simultaneously. A comparison of the detected minerals is given in table one. Pyrite and wurtzite were measured in all samples. The results for BS6 and BS7 (both matrix material) are similar and their diffraction data are dominated by sulphide peaks. The powder diffraction pattern for BS4 (greyish, yellow zone; see Fig.14) and BS5 (nest of crystals) look similar to the BS6 and BS7 counterparts, but small peaks of gypsum are present. In Sample BS3 (open conduit wall) marcasite is absent and sphalerite, wurtzite and chalcopyrite are dominant. Sample BS2 (whitish, grey zone) shows special characteristics: the powder diffraction data is dominated by gypsum and anhydrite with minor pyrite and wurtzite, while sphalerite, marcasite and chalcopyrite are absent. This mineral association indicates lower temperature and intense fluid-seawater mixing. Finally the powder diffraction data for sample BS1 contains peaks of pyrite, marcasite, sphalerite, wurtzite and galena with small peaks of barite, while no chalcopyrite was observed.

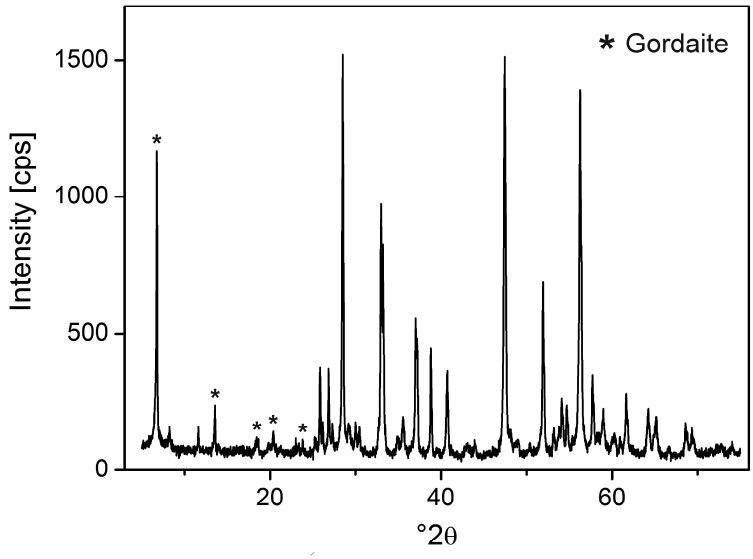

Fig. 12. X-ray powder diffraction pattern of sample BS4 (greyish, yellow zone), consisting of several minerals. The peaks marked with asterisks are assigned to gordaite.

Gordaite ($Zn_4Na(OH)_6(SO_4)Cl \cdot 6H_2O$) was observed in five samples (BS3, BS4, BS5, BS6, BS7) with the highest intensity in sample BS4 (Fig. 12). Nasdala et al. (1998) suggest that this mineral precipitates primary during fluid-seawater mixing because primary sulphates (e.g. barite) overgrew gordaite. The complete lacking of gordaite in sample BS1 (outermost, brownish zone), which was in direct contact with the seawater and in sample BS2 (whitish, grey zone, dominated by Ca sulphates), which mineral association indicates lower temperatures, suggests that the precipitation of gordaite requires elevated temperatures.

Manganite (MnOOH) was detected in five samples (BS3, BS4, BS5, BS6, BS7). However the formation of manganite is unclear. A biogenic source, like in the Mn-Fe-rich seafloor nodules, could be possible. Due to overlapping with an anhydrite peak, the detection of dolomite in sample BS2 is not totally clear.

Table 1. Distribution of mineral phases (detected by X-ray powder diffraction) among sampling sites.

Mineral	Ideal formula	BS1	BS2	BS3	BS4	BS5	BS6	BS7
Pyrite	FeS_2	×	×	×	×	×	×	×
Marcasite	FeS_2	×			×	×	×	×
Sphalerite	ZnS	×		×	×	×	×	×
Wurtzite	ZnS	×	×	×	×	×	×	×
Chalcopyrite	$CuFeS_2$			×	×	×	×	×
Galena	PbS	×						
Barite	$BaSO_4$	×						
Anhydrite	$CaSO_4$		×					
Gypsum	$CaSO_4 \cdot 2H_2O$		×		×	×		
Gordaite	$NaZn_4(OH)_6(SO_4)Cl \cdot 6H_2O$			×	×	×	×	×
Manganite	MnOOH			×	×	×	×	×
(Dolomite*)	$CaMg(CO_3)_2$		×					
(Palygorskite*)	$(Mg.Al)_5(Si.Al)_8O_{20}(OH)_2 \cdot 8H_2O$							×

* Note that the identification of dolomite and palygorskite is not unambiguous and needs further verification.

4.3 Raman spectroscopy

Raman spectroscopy provides the unique opportunity to analyse non-destructively polished sections as well as unprepared rock samples. Only minute amounts of sample, on the order of a few cubic micrometres, are needed for the detection of fingerprint spectra. Furthermore, polymorphic minerals such as pyrite and marcasite can be discriminated (Fig. 15).

Pyrite (FeS_2) shows two dominant bands at 347 cm^{-1} (E_g vibrational mode) and 382 cm^{-1} (A_g), and a minor band at 435 cm^{-1} [$F_g(3)$; Fig 13a]. The band at 347 cm^{-1} is assigned to the displacement of the sulphur atoms perpendicular to the S–S bond (librational movement), whereas the dominant 382 cm^{-1} mode represents the in-phase and out-of-phase stretching vibrations of the S_2 dumbbells (Sourisseau et al., 1991). A minor band at 435 cm^{-1} originates from combined librational and stretching motions. Vogt et al. (1983) reported three bands at 343, 379, and 435 cm^{-1}. Comparing to these results, the two measured, dominant bands (347 and 382 cm^{-1}) show significant shifts towards higher wavenumbers. Sample-heating effects (Mernagh and Trudu 1993) or surface defects resulting from mechanical polishing, lead to broadened Raman bands with decreased band heights and up-shifted band positions (Pacevski et al. 2008; Libowitzky et al. 2011).

Two dominant marcasite (FeS_2) bands are located at 324 and 387 cm^{-1} (both are A_g modes). The minor band at 448 cm^{-1} (see Fig 13c) is possibly a B_{1g}-type mode. The two A_g and the B_{1g} vibrational modes represent mixed stretching and librational vibrations (Lutz and

Müller 1991). The marcasite Raman spectra obtained in the present MSc thesis match very well the reference spectrum; no stress-induced up-shifts like in pyrite were observed.

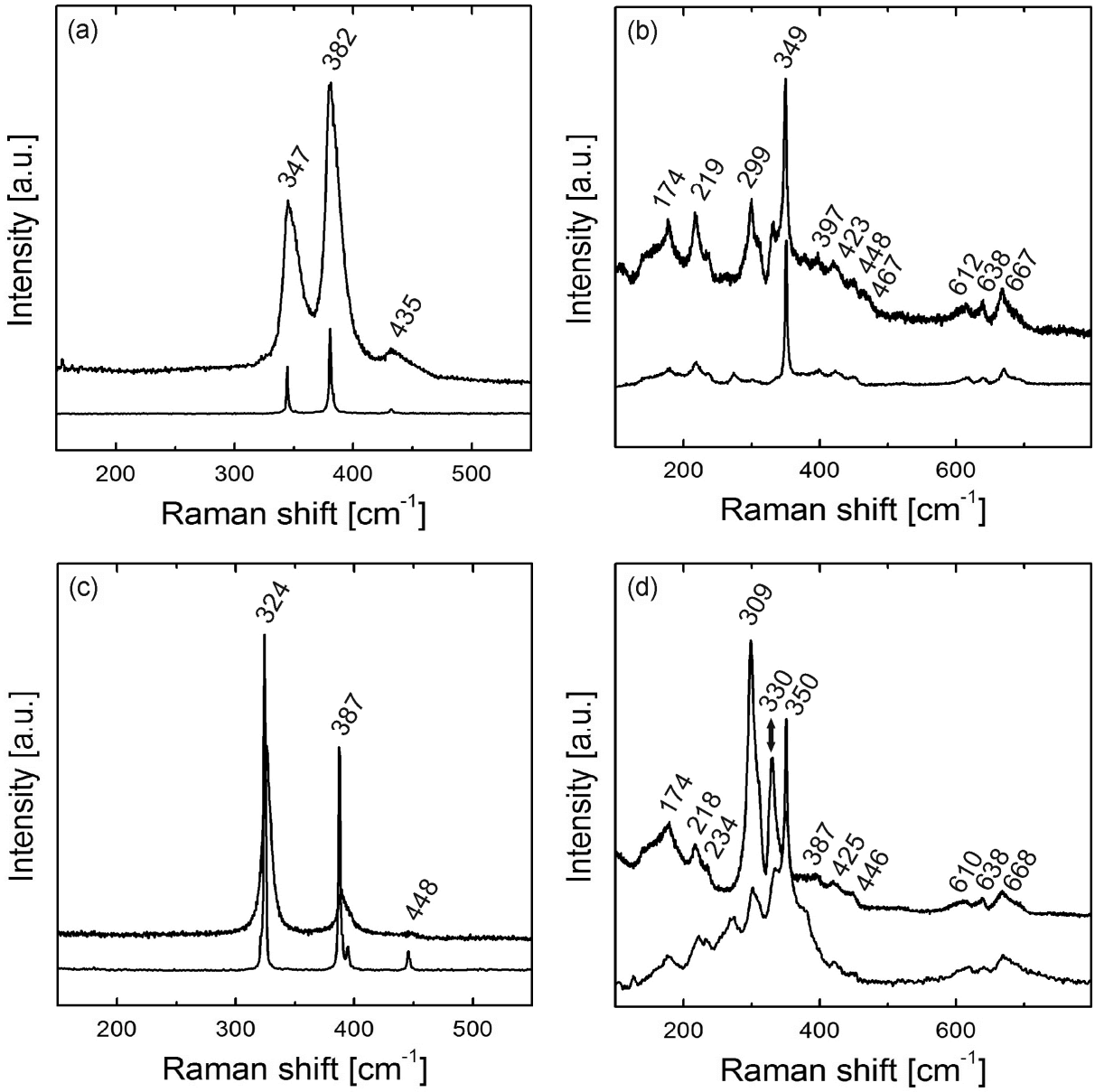

Fig. 13. Raman spectra of (**a**) pyrite, (**b**) sphalerite, (**c**) marcasite, and (**d**) wurtzite (top spectra) in comparison with references (shown below). Three of the reference spectra were extracted from the RRUFF^{TM} database (www.rruff.info: pyrite, #R100166; sphalerite, #R050140; marcasite, #R060882).

The sphalerite (ZnS) spectrum (Fig. 13b) is dominated by intense bands at 174, 219, 299, and 349 cm^{-1} and several shoulder-like, weak humps between 400 and 500 cm^{-1}. The first-order Raman spectrum of sphalerite consists of one prominent band at 350 cm^{-1} (LO mode) and one minor band at 274 cm^{-1} (TO mode) only (Couture-Mathieu and Mathieu 1953; Nilsen 1969). All bands observed below 250 cm^{-1} are second-order modes. To give two examples, the 174 cm^{-1} band corresponds to the TA overtone and the 219 cm^{-1} band to the

LA overtone (Nilsen 1969). All other bands and unresolvable shoulders at Raman shifts above 360 cm^{-1} are probably combination bands. This assignment was for instance proposed by Nilsen (1969) for the 423 cm^{-1} (LO+TA) and the 638 cm^{-1} band (TO+LO). The prominent band at 299 cm^{-1} corresponds to the so called Y_1 mode, which originates from elevated Fe contents (Sandoval et al. 2003).

Previous studies on wurtzite (ZnS) reported two bands at $A_1(TO) = E_1(TO) = 273$ cm^{-1} and $A_1(LO) = E_1(LO) = 351$ cm^{-1} (Brafman and Mitra 1968) with a strong orientation dependence of the $A_1(TO) = E_1(TO) = 273$ cm^{-1} band (Arguello et al. 1969). However measured wurtzite shows three prominent bands at 309, 330, and 350 cm^{-1} (Fig. 13d) with a sharp $A_1(LO) = E_1(LO) = 350$ cm^{-1} mode. The two strong bands at 309 and 330 cm^{-1} originate possibly from elevated Fe-contents (Mernagh and Trudu 1993). The bands at 174, 218, 234, 387, 425, 446, 610, 638, and 668 cm^{-1} are overtones and combined vibrations, similar to those bands in the sphalerite spectrum.

The chalcopyrite ($CuFeS_2$) spectrum is dominated by an intense band at 290 cm^{-1} (Fig. 14). Three minor bands at 319, 353 and 379 cm^{-1} are also detected. The band positions obtained in the present MSc thesis are in good agreement with values measured in earlier studies on this mineral: Ohrendorf and Haeuseler (1999) have reported 293 cm^{-1} for the A_1 mode, and 322, 352, and 378 cm^{-1} for the B_2 and E modes of chalcopyrite.

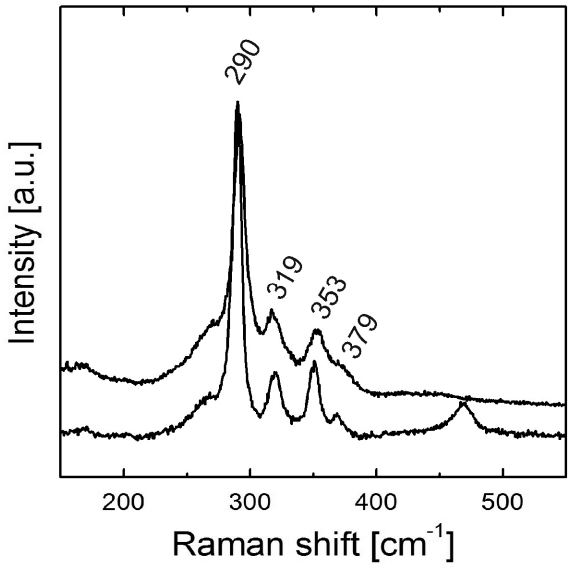

Fig. 14. Raman spectrum of chalcopyrite (top) along with a reference spectrum (www.rruff.info: #R050018; bottom).

Native sulphur (α-S) shows a prominent, narrow band at 217 cm^{-1} (Fig. 15). Minor bands occur at 151, 246, 434, and 471 cm^{-1}. All bands in the 100–300 cm^{-1} region are

assigned to bending movements within the S_8 molecule, whereas the bands in the 400–500 cm^{-1} range originate from S–S stretching vibrations (Harvey and Butler 1986).

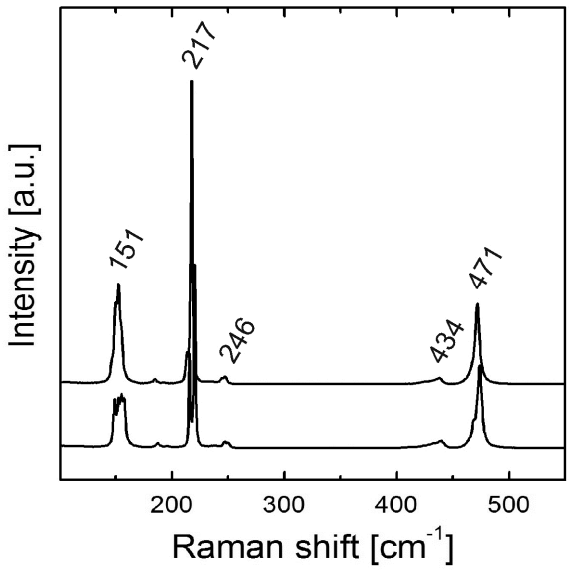

Fig. 15. Raman spectrum of native sulphur (top) along with a reference spectrum (bottom).

In general, Raman spectra of sulphates are dominated by internal vibrations of the SO_4 groups. The symmetric stretching of the tetrahedrons [$\nu_1(SO_4)$; ~1000 cm^{-1}] causes the most intense band. Their asymmetric stretching [$\nu_3(SO_4)$] is typically observed at higher Raman shifts (~1100–1200 cm^{-1}) whereas the internal SO_4 bending modes have somewhat lower energies. In-plane bending of O–S–O angles within tetrahedrons [$\nu_2(SO_4)$] movements occur around 400–500 cm^{-1} whereas out-of-plane bending motions [$\nu_4(SO_4)$] are typically observed near 600–700 cm^{-1} (Siebert 1966; Smith and Carabatos-Nédelec 2001; Nasdala et al. 2004; White 2008).

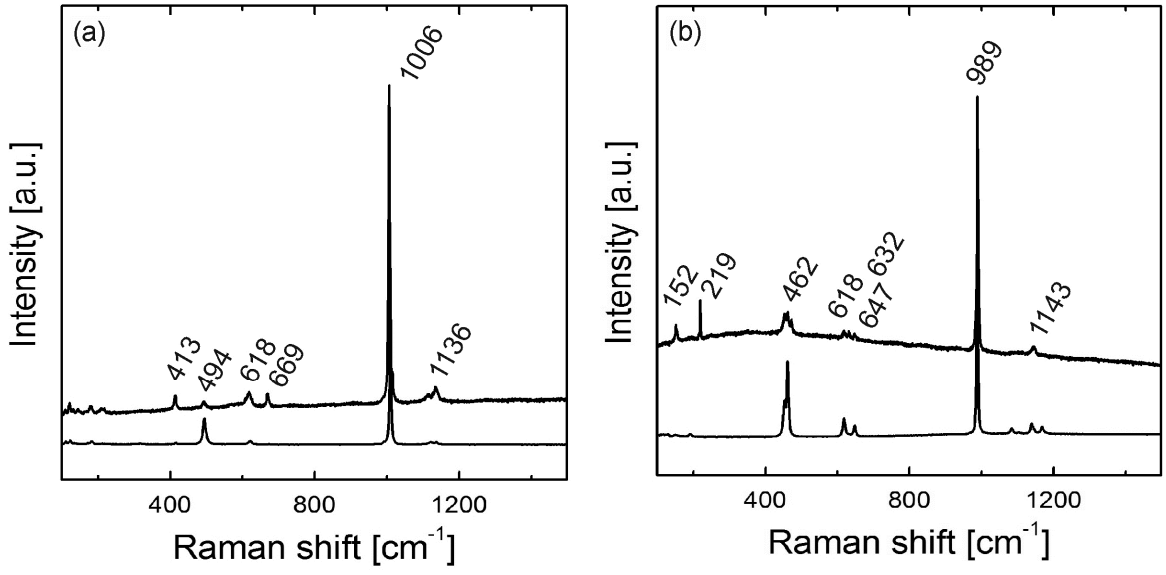

Fig. 16. Raman spectra of (**a**) gypsum and (**b**) barite (top) along with reference spectra (bottom). Note that the 152 and 219 cm^{-1} bands in the barite spectrum are due to the presence of minute amounts of native sulphur.

The Raman spectrum of gypsum ($CaSO_4 \cdot 2H_2O$; Fig. 16a) consists of a prominent band at 1006 cm^{-1} (ν_1) and minor bands at 413, 494 (ν_2), 618, 669 (ν_4), and 1136 cm^{-1} (ν_3). Barite ($BaSO_4$; Fig. 16b) shows a major band at 989 cm^{-1} (ν_1) and minor bands at 454, 462, 472 (ν_2), and 618, 632, 647 (ν_4), 1143 cm^{-1} (ν_3)

The most intense band of goslarite ($ZnSO_4 \cdot 7H_2O$) is located at 1022 cm^{-1} and several minor bands occur at Raman shifts above 1000 cm^{-1} (Fig. 17). At lower wavenumbers seven bands are detected: 221, 279, 422, 504, 626, 666, and 908 cm^{-1}. According to the results of Buzgar et al. (2009), the following bands are ascribed to internal movements of the SO_4 tetrahdrons: 1022 cm^{-1} to $\nu_1(SO_4)$; 422, 504 cm^{-1} to $\nu_2(SO_4)$; 1070, 1190 cm^{-1} to $\nu_3(SO_4)$; 626, 666 cm^{-1} to $\nu_4(SO_4)$. Additional bands, i.e. those not related to internal SO_4 vibrations, were reported by Buzgar et al. (2009) at 223 and 281 cm^{-1}. Chio et al. (2007) also described three bands with Raman shifts between 200 and 300 cm^{-1} for melanterite ($FeSO_4 \cdot 7H_2O$). These authors discussed that those three bands possibly due to movements of distorted FeO_6 octahedrons formed by Fe ions and free water molecules. Buzgar et al. (2009) concluded that the two goslarite bands below 300 cm^{-1} are, in analogy to melanterite, due to interaction of Zn with the oxygen atoms of free water molecules.

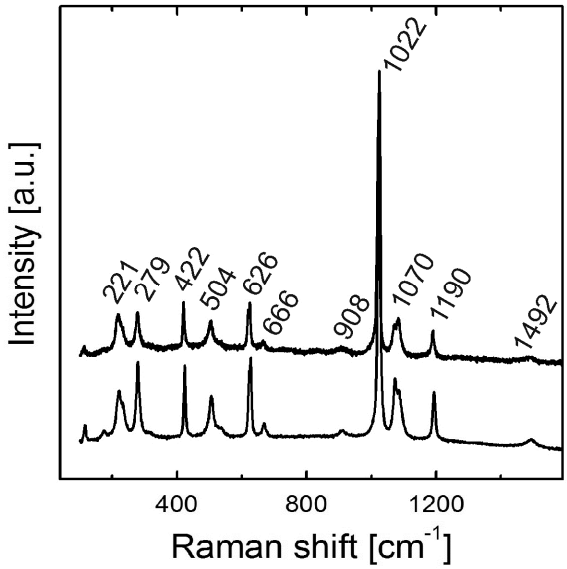

Fig. 17. Raman spectrum of goslarite (top) along with a reference spectrum (bottom).

The Raman spectrum of jôkokuite ($MnSO_4 \cdot 5H_2O$) is dominated by an intense band at 1019 cm^{-1} (Fig. 18). It shows similarities to the goslarite spectrum; however some of the

minor bands have notably different Raman-shift values. Weak bands occur at 219, 272, 422, 496, 620, 662, 1090, and 1193 cm^{-1}. Band assignment is difficult, because neither Raman spectroscopic studies nor Raman spectroscopic calculations on jôkokuite have been published so far. The following bands are probably ascribed to internal movements of SO_4 tetrahedrons: 1019 cm^{-1} to $\nu_1(SO_4)$; 422 and 496 cm^{-1} to $\nu_2(SO_4)$; 1090 and 1193 cm^{-1} to $\nu_3(SO_4)$; and 620 and 662 cm^{-1} to $\nu_4(SO_4)$. The Mn ions are octahedrally coordinated by six oxygen atoms, four of which belong to water molecules and two to sulphate groups (Caminiti et al. 1982). Therefore it is likely that the bands at 219 and 272 cm^{-1} originate from the interaction of manganese with the oxygen atoms of the free water molecules.

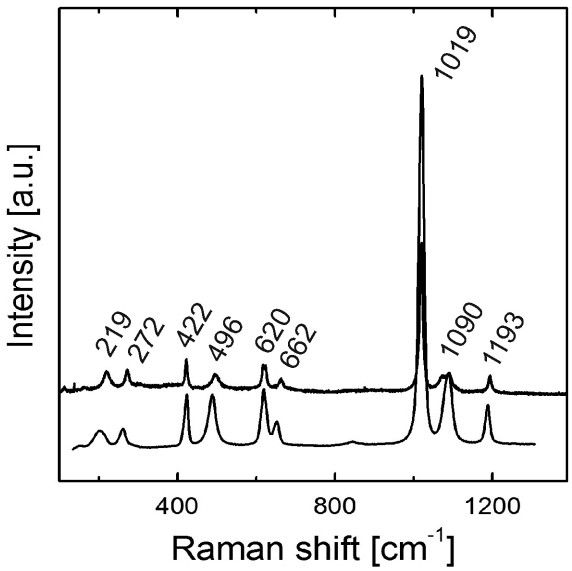

Fig. 18. Raman spectrum of jôkokuite (top) along with a reference spectrum (www.rruff.info: #R070102; bottom).

Metavoltine ($Na_6K_2FeFe_6(SO_4)_{12}O_2 \cdot 18H_2O$) yields two intense bands at 266 and 1009 cm^{-1}; a number of additional minor bands occur at Raman shifts above 1000 cm^{-1} (Fig. 19). The following bands are detected in the low Raman-shift region: 183, 338, 372, 444, 499, 559, and 611 cm^{-1}. Results of earlier Raman spectroscopic studies are not available and band assignment is therefore difficult. The structure of metavoltine is quite complex and shows a layered composition. Octahedrally coordinated Fe^{3+} ions form $Fe_3^{3+}O(H_2O)_3(SO_4)_6$ clusters which are linked by K and Na. The layers are connected via hydrogen bonds through layers of H_2O groups belonging to isolated $Fe^{2+}(H_2O)_6$ octahedrons (Giacovazzo et al. 1976). The following bands are probably ascribed to movements of the SO_4 tetrahdrons: 1009 cm^{-1} to $\nu_1(SO_4)$; 444 and 499 cm^{-1} to $\nu_2(SO_4)$; 1056, 1112, and 1174 cm^{-1} to $\nu_3(SO_4)$; and 559 and 611 cm^{-1} to $\nu_4(SO_4)$. All bands below 300 cm^{-1}, including a strong mode at 266 cm^{-1},

originate possibly from movements of the isolated $Fe^{2+}(H_2O)_6$ octahedrons. The sharp bands at 338 and 372 cm^{-1} are lacking in the reference spectrum (Fig. 19). They are tentatively assigned to minor sample contamination with ion sulphide.

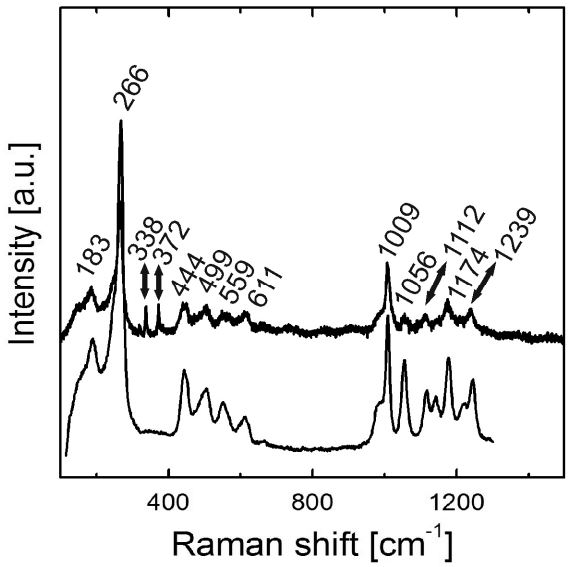

Fig. 19. Raman spectrum of metavoltine (top) along with a reference spectrum (www.rruff.info: #R060835; bottom). Two bands at 338 and 372 cm^{-1} are assigned to FeS_2 present in the sample (compare spectra shown in Fig. 13).

4.3 Chemical analyses

For some major elements (Ba, Cu, Zn, Ca, Fe) both NAA and ICP-OES were applied. The results (Table 2) fit adequately, however sample heterogeneities and measuring inaccuracies may cause differences. Some trace elements (As, Cd, Co, Ga, Mo, Sb) are measured by both NAA and ICP-MS. The results (Table 3) are in good agreement, however some significant differences (e.g. As in sample BS5) occur owing to sample heterogeneities and measuring inaccuracies.

The major element chemistry of the different samples varies remarkably (Table 2). Only iron, zinc and sulphur are major elements in all seven samples. The Fe content ranges between 4.9 and 34.3 % and the Zn content varies between 6.5 and 53.1 %. Sulphur was not measured quantitatively owing to incomplete digestion of anhydrite and barite; however it is assumed that sulphur occurs as major element in all samples. Moreover copper (Cu 0.3–2.9 %) and calcium (Ca 0.1–18.1 %) are detected in major or minor amounts in all samples. The Ba content varies between 7 ppm (BS7, matrix material) and 3.6 % (≙36000 ppm; BS1, outermost brownish zone). The Pb content ranges from 407 ppm to 1.1 % (≙11000 ppm). The

Si content for sample BS3 (open conduit wall) is below detection limit (<0.01 %), whereas in sample BS1 (outermost brownish zone) Si (9.3 %) is the fourth most abundant element. The elements Al, Mg, K and P occur only in minor or trace amounts and are often below detection limit (see table 2).

The major element chemistry reflects the phase composition of different samples. The results point out impressively that barite is only stable at lowest temperature zones. Therefore Ba is in the outermost zone (BS1) ~5100 times more abundant than in the matrix sample BS7. The elevated Ca content in sample BS2 originates from the plenty occurrence of anhydrite and gypsum. Anhydrite builds up the initial chimney wall and separates seawater and hydrothermal fluid firstly. At the anhydrite-seawater interface small fluid inclusions precipitate which form pyrite, marcasite, galena, sphalerite, wurtzite and barite (Haymon 1983). Sample BS1 reflects the composition of this "outermost skin". At the anhydrite-fluid interface, a mixture of coarse-grained pyrite, marcasite, sphalerite, wurtzite and chalcopyrite precipitates (BS4–BS7). The hottest area (i.e. open conduit wall; sample BS3) mainly consists of wurtzite and chalcopyrite with a high Zn and Cu content and low Fe, Ba, Pb and Si contents. Amorphous silica (SiO_2) represents the main source for silicon. Chemical investigations are, beside scanning electron microscopy, the only way to prove the presence of this phase. Elevated Si contents are observed in sample BS1 (9.3 %) and BS4 (1.4 %).

Table 2. Analytical results for major and minor elements. All values are in wt%.

	Mg	Al	Si	P	K	Ca		Fe	
	OES	OES	OES	OES	OES	OES	NAA	OES	NAA
BS1 (outermost brownish zone)	(bdl)	0.7	9.3	(bdl)	0.2	0.3	0.2	23.0	21.9
BS2 (whitish grey zone)	(bdl)	0.2	0.4	0.008	(bdl)	9.9	18.1	10.6	4.9
BS3 (open conduit wall)	(bdl)	(bdl)	(bdl)	(bdl)	(bdl)	0.2	0.4	8.8	8.5
BS4 (greyish yellow zone)	(bdl)	0.8	1.4	(bdl)	(bdl)	0.3	0.3	33.2	34.3
BS5 (nest of crystals)	(bdl)	0.03	0.1	(bdl)	(bdl)	0.2	0.2	22.4	11.0
BS6 (matrix material)	(bdl)	(bdl)	0.03	0.006	(bdl)	0.2	0.1	12.4	11.9
BS7 (matrix material)	0.3	0.1	0.2	(bdl)	(bdl)	0.2	0.1	16.2	15.8
Detection limit OES	0.01	0.01	0.01	0.005	0.1	0.1		0.05	

Table 2. continued

	Cu		Zn		Ba		Pb
	OES	NAA	OES	NAA	OES	NAA	OES
BS1 (outermost brownish zone)	0.3	0.3	11.4	10.8	3.6	3.2	1.1
BS2 (whitish grey zone)	1.0	0.3	22.8	6.5	0.1	0.05	0.2
BS3 (open conduit wall)	2.1	2.0	53.1	49.7	0.002	0.01	(bdl)
BS4 (greyish yellow zone)	0.5	0.3	12.1	8.6	0.003	0.01	0.2
BS5 (nest of crystals)	2.2	2.9	31.9	41.4	0.01	0.01	0.1
BS6 (matrix material)	2.3	2.3	45.3	43.5	(bdl)	0.01	0.1
BS7 (matrix material)	1.3	1.3	39.5	37.6	(bdl)	0.01	0.2
Detection limit OES	0.005		0.01		0.001		0.01

NAA = Neutron activation analysis; OES = Inductively-coupled plasma optical emission spectroscopy.
Note that Ti is below the detection limit in all samples (<0.01 %).

The trace element chemistry points out the extensive heterogeneities of the different samples (Table 3). The most abundant trace elements are sodium (Na 355–2350 ppm), manganese (Mn 800–2440 ppm), cadmium (Cd 161–2140 ppm) and arsenic (As 99–1220 ppm). Moreover strontium is strongly enriched in sample BS1 (1630 ppm), whereas the Sr content in sample BS7 decreases to 7 ppm. Large ions like strontium, rubidium (Rb 0.4–11 ppm) and caesium (Cs <0.1–1.3 ppm) are mainly incorporated in barite and therefore their contents are linked to the abundance of barite. All of these four elements reach their peak concentration in sample BS1 consequently.

The presence of gordaite as main phase in some samples explains the high Na contents (355–2350 ppm). However in sample BS1 (Na = 2010 ppm) gordaite is absent (see chapter 5.2) and the high Na concentration is probably linked to small halite (NaCl) crystals, which precipitate during sample recovery and drying at air. Furthermore elevated As (99–1220 ppm) and Sb (13–99 ppm) concentrations may originate from submicroscopic inclusions of primary tennantite $\{Cu_{12}[S(AsS_3)_4]\}$.

Cadmium (Cd 161–2140 ppm), gallium (Ga 17–135 ppm) and selenium (Se 10–41 ppm) are mainly incorporated in the Zn sulphides and therefore they reach peak concentrations in Zn-rich samples. Elevated Mn concentrations range between 800 and 2440 ppm, but no clear trend is observed, as manganese is incorporated in both FeS_2 and zinc sulphides in greater amounts. The presence of manganite and jôkokuite increases the Mn content remarkably. However manganese reaches the lowest concentration in the Zn-rich sample BS3. The Tl concentration (17–576 ppm) is obviously linked to the Mn content and reaches, similar to manganese, the peak concentration in sample BS4 consequently. Thallium shows a complex geochemical behaviour: during reducing conditions thallium occurs as Tl^+ ion with a similar size to the heavier alkali metals (K, Rb, Sr). Therefore it substitutes potassium in some silicates (micas, K-feldspar); however Tl^+ is more sensitive to covalent bonding than the alkali metals and it gets incorporated into sulphide minerals too (Heinrichs et al. 1980; Coggon et al. 2014). In oceanic systems an uptake of Tl^+ from seawater by ferromanganese minerals occurs (Rehkämper et al. 2002; Rehkämper and Nielsen 2004). Thallium forms surface sorption complexes at the ferromanganese mineral surfaces, which is, depending on the manganese mineral, sometimes accompanied by an oxidation to Tl^{3+} (Peacock and Moon, 2012; Nielsen et al., 2013). The strong Tl affinity to manganese minerals explains possibly the similar concentration trend of manganese and thallium.

The geochemical behaviour of uranium and vanadium is quite complex: they are derived from the seawater and therefore these elements are enriched in zones with a strong

seawater influence. Butler and Nesbitt (1999) suggest that uranium and vanadium are concentrated by an efficient redox trap mechanism on mineral surfaces at the fluid-wall interface. Whether this process is catalysed by microorganisms or not, is still subject to discussion. For molybdenum (Mo 41–306 ppm), germanium (Ge 11–41 ppm), cobalt (Co <0.2–37 ppm) and nickel (Ni <10–15 ppm) no clear concentration trends are observed and it is expected that they are incorporated in many different phases.

The precious metals silver (Ag 26–511 ppm) and gold (Au 1.1–15.3 ppm) are detected in measurable quantities in all samples. Argentiferous, submicroscopic inclusions of tennantite in galena and Zn sulphides could be the main source for silver. Submicroscopic, native gold inclusions occur probably in sphalerite and chalcopyrite. Moss and Scott (2001) investigated Au-rich samples from the eastern Manus basin and reveal that gold inclusions, visible in reflected light, occur in tennantite and in a late generation of chalcopyrite. Herzig et al. (1993) reported gold inclusions in sphalerite and chalcopyrite from Zn-rich chimneys from the Lau back arc basin. They show that the highest Au concentrations are found in low temperature sphalerite-barite mineral assemblages. Precipitation of native gold happens during initial stages of mixing with seawater at temperatures down to 230 °C and is restricted to the inner margins of the mixing zone (Herzig et al. 1993). The barite rich sample BS1 (13 ppm; outermost, brownish zone) and sample BS4 (15.3 ppm; greyish, yellow zone) show the highest measured Au concentrations. Following this, it is likely that these samples represent the inner margins of the early mixing zone. Moreover the Au concentrations correlate well with the Ag, As and Sb contents (see table 3).

Table 3. Analytical results for trace elements. All values are in parts per million (ppm; NAA results for La and U in ppb).

	Na NAA	V MS	Mn MS	Co MS	Co NAA	Ni MS	Ga MS	Ga NAA	Ge MS	As MS	As NAA
BS1 (outermost brownish zone)	2010	26	1700	(bdl)	0.3	15	43	35	41	907	848
BS2 (whitish grey zone)	355	15	905	1.4	1.7	(bdl)	87	18	11	185	111
BS3 (open conduit wall)	745	(bdl)	800	37.0	35.0	(bdl)	120	78	14	125	99
BS4 (greyish yellow zone)	2350	86	2440	2.1	1.5	10	30	17	34	1200	1220
BS5 (nest of crystals)	1360	(bdl)	1520	15.0	10.0	(bdl)	72	104	17	559	116
BS6 (matrix material)	1070	(bdl)	1140	26.0	21.0	(bdl)	104	89	12	206	178
BS7 (matrix material)	709	26	1460	(bdl)	0.2	(bdl)	135	118	25	377	344
Detection limit MS		5	3	0.2		10	0.2		0.7	5	

Table 3. continued

	Se MS	Rb MS	Sr MS	Mo MS	Mo NAA	Ag NAA	Cd MS	Cd NAA	Sn MS	Sb MS	Sb NAA
BS1 (outermost brownish zone)	10	11.0	1630	306	270	511	161	164	(bdl)	99	93
BS2 (whitish grey zone)	16	0.4	546	95	41	82	752	255	(bdl)	20	13
BS3 (open conduit wall)	37	0.4	10	74	50	26	2110	2140	(bdl)	20	18
BS4 (greyish yellow zone)	12	1.3	17	228	218	228	291	199	0.8	31	24
BS5 (nest of crystals)	33	0.4	13	87	122	71	1460	2070	(bdl)	16	25
BS6 (matrix material)	41	0.5	7	99	105	61	1910	1960	(bdl)	15	16
BS7 (matrix material)	34	0.6	6	206	175	137	1160	1130	(bdl)	39	33
Detection limit MS	0.8	0.4	3	1			2		0.5	2	

Table 3. continued

	Cs MS	Ba MS	La NAA**	Ce MS	Nd MS	Au NAA	Tl MS	Pb MS	Th MS	U NAA**
BS1 (outermost brownish zone)	1.3	(>10000)*	254	(bdl)	0.5	13.0	513	(>5000)*	0.3	517
BS2 (whitish grey zone)	(bdl)	1110	222	(bdl)	(bdl)	2.3	64	1400	(bdl)	219
BS3 (open conduit wall)	0.1	34	56	(bdl)	(bdl)	1.1	17	407	(bdl)	884
BS4 (greyish yellow zone)	0.5	50	37	(bdl)	(bdl)	15.3	576	1890	(bdl)	635
BS5 (nest of crystals)	(bdl)	154	595	(bdl)	(bdl)	1.9	190	1170	(bdl)	648
BS6 (matrix material)	(bdl)	12	596	1.9	1.6	2.7	64	1120	0.1	713
BS7 (matrix material)	(bdl)	7	56	(bdl)	(bdl)	5.7	95	2080	(bdl)	303
Detection limit for MS	0.1	3		0.8	0.4		0.1	0.8	0.1	

NAA = Neutron activation analysis; MS = Inductively-coupled plasma mass spectrometry; (bdl) = below detection limit.
The following elements analysed were below the respective detection limit in all samples: Er, Eu, Gd, Pr, Sm, Tb, Tm, Y, and Yb (<0.1 ppm); Ho, In, and Ta (<0.2 ppm); Dy (<0.3 ppm); W (<0.7 ppm); Bi (<2 ppm); Nb (<2.4 ppm); Li (<3 ppm); Be (<4 ppm); Te (<6 ppm); Cr (<30 ppm).
* In BS1, barium and lead could not be quantified because the content was above the upper detection limit of the MS technique
** Note that NAA results for La and U are quoted in parts per billion (ppb).

4.5 Phase relationships and growth history

During initial chimney growth, an anhydrite rich layer builds up, which separates seawater and hydrothermal fluid firstly. At the anhydrite-seawater interface small fluid inclusions precipitate, forming small pyrite, marcasite, galena, sphalerite, wurtzite and barite grains (Haymon 1983). Reflected light microscopy shows that pyrite and marcasite crystallise at the earliest, because they are corroded or coated by early Zn sulphides, galena and barite. At the anhydrite-fluid interface a mixture of coarse-grained pyrite, marcasite, sphalerite, wurtzite and chalcopyrite precipitates. The deposition sequence corresponds to an initial growth of pyrite ± marcasite followed by the simultaneous precipitation of Zn sulphides and chalcopyrite. The hottest area (i.e. open conduit wall) consists of dendritic, saw-blade-like wurtzite crystals with fine grained, euhedral chalcopyrite inclusions, which may grow simultaneously. Thermodynamic calculations for the mineralisation of sphalerite and wurtzite reveal saturation temperatures of 275–285 °C, which are significant higher than in other locations (e.g. Main Endeavour and Mothra vent field, Juan de Fuca Ridge) owing to the higher pH value (Carddock 2009). For chalcopyrite Carddock (2009) calculates saturation temperatures of about 300–310 °C for the "Vienna Woods" hydrothermal field. Moreover gordaite precipitates primary during fluid-seawater mixing (Nasdala et al. 1998). However the absence of gordaite in samples BS1 (outermost zone) and BS2 (whitish, grey zone; anhydrite-rich layer), suggests that gordaite only grows at the anhydrite-fluid interface. It is possible that gordaite precipitates as seawater enters the porous chimney and mixes with the hydrothermal fluid. Native sulphur was observed in samples BS1, BS2 and BS7, but a biologically triggered precipitation is supposed.

Raman spectroscopy and X-ray powder diffraction show that in sample BS2 (whitish grey zone), which represents the initial anhydrite wall, hydration of anhydrite leads to the formation of gypsum. Moreover jôkokuite is associated with goslarite and metavoltine, but it precipitates probably as primary phase firstly. Synthetic $MnSO_4 \cdot 5H_2O$ crystallises between 9 and 24 °C, whereas synthetic $MnSO_4 \cdot 7H_2O$ (between –10 and 9 °C) and $MnSO_4 \cdot 4H_2O$ (>27.5–60 °C) occur at different temperatures (Kemmit and Peacock 2013). The temperature range for $MnSO_4 \cdot 5H_2O$ is higher than the bottom seawater temperature (3 °C); therefore jôkokuite precipitates during post hydrothermal alteration by seawater. This assumption suggests that jôkokuite forms primary during fluid-seawater mixing at low temperatures. Otherwise goslarite ($ZnSO_4 \cdot 7H_2O$) grows secondary as alteration product from Zn sulphides. Experiments on synthetic $ZnSO_4 \cdot 7H_2O$ show that goslarite gets highly soluble in water by

increasing temperature. It is even at room temperature hardly stable (Saha and Podder 2011). This assumption suggests that goslarite has not precipitated simultaneously with jôkokuite and its formation is secondary, probably at ambient seawater temperature. Furthermore manganite (MnOOH) was detected in five samples (BS3, BS4, BS5, BS6, BS7) by X-ray powder diffraction. However the formation of manganite is unclear. A biogenic source, like in the Mn-Fe-rich seafloor nodules, is possible. The growth conditions of metavoltine on FeS_2 surfaces are not known, since no published data have been available. However it is likely that metavoltine forms secondary during low temperature alteration. Finally the detection of palygorskite and dolomite by X-ray powder diffraction is not unambiguous clear, and a contamination during sample recovery seems likely.

5. Conclusion

This MSc thesis examines and characterises the mineralogical relationships and chemical composition of a “black smoker” fragment, taken from an active chimney. Beside phase analyses of powder samples, space resolved analyses of both, thick couples and unprepared rock samples are used to characterise gangue material, secondary minerals and sulphide ores properly. A stepwise, pictorial documentation gives an excellent overview of mineral associations at different scales. Reflected light images show phase relationships and growth cycles between ore minerals. With detailed SEM-studies different phases and crystal forms of ores, gangue material and secondary minerals are discriminated. Moreover the bulk composition has been measured by X-ray powder diffraction, which confirms the presence of gordaite as main phase in four samples. Unfortunately no Raman spectrum of gordaite could be obtained. However rare sulphate minerals like jôkokuite or metavoltine are detected by fingerprinting Raman spectroscopic measurements (Table 4). Raman spectroscopic investigations show that low temperature alteration leads to the formation of metavoltine and goslarite. Chemical analyses of major, minor and trace elements point out the heterogeneities of the different samples significantly. The successful correlation between trace elements and abundant phases confirms previous observations. The results for the precious metals Ag and Au yield the expected enrichment; however no native gold inclusions are visible in reflected light.

In summary the mixture of analyses methods has been effective and the occurrence of at least six new minerals for the locality “Vienna Woods” is presented in this work (Table 4). Raman spectroscopy is a suitable technique for detecting both sulphides and sulphates at small scale. Therefore powerful-sea going Raman systems have got a great potential in marine geosciences, as they offer the opportunity to measure metastable phases in-situ on chimney walls. However some current problems, like technical limitations and lacking reference spectra must be overcome. Further attention needs to be paid on the phase relationship between pyrite and marcasite, because no clear growth history can be defined. Moreover the formation of manganese minerals (manganite, jôkokuite) is poorly understood.

Table 4. List of all mineral phases detected. along with the respective techniques.

Mineral	Ideal formula	RMS	PXRD	RLM	SEM
Pyrite	FeS_2	×	×	×	
Marcasite	FeS_2	×	×	×	
Sphalerite	ZnS	×	×	×	
Wurtzite	ZnS	×	×	×	×
Chalcopyrite	$CuFeS_2$	×	×	×	
Galena	PbS		×	×	
Sulphur	α-S	×			×
Barite	$BaSO_4$	×	×		
Anhydrite	$CaSO_4$		×		
Gypsum*	$CaSO_4 \cdot 2H_2O$	×	×		×
Jôkokuite*	$MnSO_4 \cdot 5H_2O$	×			
Goslarite*	$ZnSO_4 \cdot 7H_2O$	×			
Gordaite*	$NaZn_4(OH)_6(SO_4)Cl \cdot 6H_2O$	×	×		×
Metavoltine*	$Na_6K_2FeFe_6(SO_4)_{12}O_2 \cdot 18H_2O$	×			
Amorphous silica	SiO_2				×
Manganite*	MnOOH		×		
(Dolomite*)	$CaMg(CO_3)_2$		×		
(Palygorskite*)	$(Mg.Al)_5(Si.Al)_8O_{20}(OH)_2 \cdot 8H_2O$		×		

RMS = Raman micro-spectroscopy; PXRD = powder X-ray diffraction; RLM = reflected-light optical microscopy; SEM = energy-dispersive X-ray analysis in the scanning electron microscope.
* First find for the "Vienna Woods" hydrothermal field.
Note that the identification of dolomite and palygorskite is not unambiguous and needs further verification.

Appendix I: List of figures

Fig. 1. Formation of vent fluids in mid-ocean-ridges (simplified sketch; modified after Tivey 2007). 1

Fig. 2. Photograph of an active black smoker chimney in the southern part of the East Pacific Rise, taken from the submersible Alvin (**a**). Photograph of a diffuse venting spire in the "Vienna Woods" vent field, Manus basin (**b**). Both images modified after Tivey (2007). 4

Fig. 3. Simplified map showing the location of the hydrothermal field "Vienna Woods" in the Manus Basin (modified after Reeves et al. 2011). 6

Fig. 4. Impressions from the hydrothermal field "Vienna Woods". (**a**) Photograph taken from the submersible *Mir 1* showing an active chimney which is covered by snails (*Olgaconcha Tufari* and *Alviniconcha cf. hessleri*), barnacles (*eochionelasmus ohtai*), sea cucumbers (*Chiridota hydrothermica*) and crabs (*Munidopsis cf. marianica*) (image courtesy of Werner Tufar). (**b**) Schematic drawing of chimneys in the "Vienna Woods" field (modified after Lisitsyn et al. 1993). 7

Fig. 5. Impressions from the 1990 research cruise OLGA II. (**a**) Research vessel "Sonne" in the port of Rabaul, New Britain (modified after Tufar 1991). (**b**) May 12, 1990: Werner Tufar on board of "Sonne", with a fragment of a just recovered, black smoker chimney, weighing ca. 1500 kilograms (image courtesy of Prof. Tufar). 9

Fig. 6. Photographs of the black smoker sample. Small green pins mark the sampling sites (cf. labels). (**a**) View onto the base (i.e. along the former venting direction). The position of BS1 at the top of the specimen cannot be seen directly; it is indicated by a black arrow. (**b**) View at the top side. Note that the surface of the black smoker, which was in direct contact with cold seawater, shows alteration indicated by light, brownish colours. (**c**) View at the bottom which shows fairly large conduits (black holes). (**d**) Open conduit wall at the bottom of the black-smoker specimen (sampling site BS3). (**e**) A nest of well-shaped crystals within the porous, fine grained matrix (sampling site BS5). 12

Fig. 7. Reflected-light photomicrographs of common mineral associations. (**a**) Cross section of the outermost, light brownish zone (BS1): dendrites of pyrite-marcasite (light yellow) in a matrix of amorphous SiO_2 and barite (red arrows) rich nodules (dark grey, black rounded areas, compare Fig. 10a). (**b**) Intergrowth of galena (light grey), sphalerite (dark grey) and pyrite (light yellow). (**c**) Chalcopyrite (yellow) inter-grown with ZnS (grey) and minor pyrite (light yellow), indicating elevated formation temperatures. (**d**) Transition zone of different mineral associations: a zone dominated by dendrites of FeS_2 (light yellow) adjoins a zone rich

in ZnS (dark grey) and chalcopyrite (yellow). Round, black areas are empty pores in the sample. 17
Fig. 8. Reflected-light photomicrographs of rare mineral associations. (**a**) Elongated borehole representing a biogenic trace (BS7). (**b**) Oriented inter-growth of dendritic ZnS (grey) with a multitude of fine-grained, idiomorphic chalcopyrite crystals (yellow; BS3). 17
Fig. 9. Secondary electrons images of typical mineral associations. (**a**) And (**b**) ZnS crystals (piled pseudohexagonal grains, columnar crystals) in a matrix of fine grained barite and amorphous silica (BS7). (**c**) Barite-rich nodules (surface of BS1; compare Fig. 8a). (**d**) Lath-shaped and rhomboidal gypsum and anhydrite crystals (BS2). 18
Fig. 10. (**a**) And (**b**) Secondary electrons images of tabular ZnS crystals overgrown by amorphous silica spherules (BS1). 19
Fig. 11. Secondary electrons image of gordaite layers (sample BS5). 20
Fig. 12. X-ray powder diffraction pattern of sample BS4 (greyish, yellow zone), consisting of several minerals. The peaks marked with asterisks are assigned to gordaite. 21
Fig. 13. Raman spectra of (**a**) pyrite, (**b**) sphalerite, (**c**) marcasite, and (**d**) wurtzite (top spectra) in comparison with references (shown below). Three of the reference spectra were extracted from the RRUFF^{TM} database (www.rruff.info: pyrite, #R100166; sphalerite, #R050140; marcasite, #R060882). 23
Fig. 14. Raman spectrum of chalcopyrite (top) along with a reference spectrum (www.rruff.info: #R050018; bottom). 24
Fig. 15. Raman spectrum of native sulphur (top) along with a reference spectrum (bottom). 25
Fig. 16. Raman spectra of (**a**) gypsum and (**b**) barite (top) along with reference spectra (bottom). Note that the 152 and 219 cm^{-1} bands in the barite spectrum are due to the presence of minute amounts of native sulphur. 26
Fig. 17. Raman spectrum of goslarite (top) along with a reference spectrum (bottom). 26
Fig. 18. Raman spectrum of jôkokuite (top) along with a reference spectrum (www.rruff.info: #R070102; bottom). 27
Fig. 19. Raman spectrum of metavoltine (top) along with a reference spectrum (www.rruff.info: #R060835; bottom). Two bands at 338 and 372 cm^{-1} are assigned to FeS_2 present in the sample (compare spectra shown in Fig. 13). 28

Appendix II: List of tables

Table 1. Distribution of mineral phases (detected by X-ray powder diffraction) among sampling sites.....22
Table 2. Analytical results for major and minor elements. All values are in wt%. 30
Table 3. Analytical results for trace elements. All values are in parts per million (ppm; NAA results for La and U in ppb).....33
Table 4. List of all mineral phases detected. along with the respective techniques.....38

Appendix III: References

Alt J (1995) Subseafloor processes in mid-ocean ridge hydrothermal systems. In: Humphris SE, Zierenberg RA, Mullineaux LS, Thomson RE (eds.) Seafloor Hydrothermal Systems: Physical, Chemical, Biological, and Geological Interactions. AGU Monograph Series No. 91, American Geophysical Union, Washington DC, pp 85–114

Arguello CA, Rousseau DL, Porto SPS (1969) First-order Raman effect in wurtzite-type Crystals. Phys Rev 181(3):1351–1363

Auzende JM, Urabe T, Ruellan E, Chabroux D, Charlou JL, Gena K, Gamo T, Henry K, Matsubayashi O, Matsumoto T, Naka J, Nagaya Y, Okamura K (1996) "Shinkai 6500" dives in the Manus Basin: new STARMER Japanese–French program. JAMSTEC J. Deep Sea Res 12:323–334

Baross JA, Lilley MD, Gordon LI (1982) Is the CH_4, H_2 and CO venting from submarine hydrothermal systems produced by thermophilic bacteria? Nature 298:366–368

Battaglia TM, Dunn EE, Lilley MD, Holloway J, Dable BK, Marquardt BJ, Booksh KS (2004) Development of an in situ fiber optic Raman system to monitor hydrothermal vents. Analyst 129:602–606

Bau M, Dulski P (1999) Comparing yttrium and rare earths in hydrothermal fluids from the Mid-Atlantic Ridge: implications for Y and REE behaviour during near-vent mixing and for the Y/Ho ratio of Proterozoic seawater. Chem Geol 155(1):77–90

Binns RA, Barriga FJAS, Miller DJ (2007) Leg 193synthesis: anatomy of an active felsic-hosted hydrothermal system, Eastern Manus Basin, Papua New Guinea. In: Barriga FJAS, Binns RA, Miller DJ, Herzig PM (eds.) Proceedings of the ocean drilling program, Scientific Results Vol. 193. Ocean Drilling Program, pp 1–71

Bischoff JL, Seyfried WEJr. (1978) Hydrothermal chemistry of seawater from 25° to 350°C. Am J Sci 278:838–860

Both R, Crook K, Taylor B, Brogan S, Chappel B, Frankel E, Liu L, Sinton J, Tiffin D (1986) Hydrothermal chimneys and associated fauna in the Manus Back-Arc Basin, Papua New Guinea. EOS T Am Geophys Un 67:489-490

Brafman O, Mitra SS (1968) Raman effect in wurtzite- and zinc-blende-type ZnS single crystals. Phys Rev 171(3):931–934

Breier JA White SN, German CR (2010) Mineral-microbe interactions in deep-sea hydrothermal systems: a challenge for Raman spectroscopy. Philos T Roy Soc A 368:3067–3086

Brewer P G, Malby G, Pasteris JD, White SN, Peltzer ET, Wopenka B, Freeman J, Brown MO (2004) Development of a laser Raman spectrometer for deep-ocean science. Deep-Sea Res Pt I 51:739–753

Butler IB, Nesbitt RW (1999) Trace element distributions in the chalcopyrite wall of a black smoker chimney: insights from laser ablation inductively coupled plasma mass spectrometry (LA–ICP–MS). Earth Planet Sc Lett 167:335–345

Buzgar N, Buzatu A, Sanislav IV (2009) The Raman study on certain sulfates. An Stiint U Al I-Mat 55(1)5–23

Caminiti R, Marongiu G, Paschina G (1982) A comparative X-ray diffraction study of aqueous $MnSO_4$ and crystals of $MnSO_4 \bullet 5H_2O$. Z Naturforsch 37a:581–586

Chio CH, Sharma SK, Muenow DW (2007) The hydrates and deuterates of ferrous sulfate ($FeSO_4$): a Raman spectroscopic study. J Raman Spectrosc 38: 87–99

Coggon RM, Rehkämper M, Atteck C, Teagle DAH, Alt JC, Cooper MJ (2014) Controls on thallium uptake during hydrothermal alteration of the upper ocean crust. Geochim Cosmochim Ac 144:25–42

Constantinou G, Govett GJS (1973) Geology, geochemistry, and genesis of Cyprus sulfide deposits. Econ Geol 68:843–858

Converse DR, Holland HD, Edmond JM (1984) Flow rates in the axial hot springs of the East Pacific Rise (21°N): implications for the heat budget and the formation of massive sulfide deposits. Earth Planet Sc Lett 69:159-175

Corliss JB, Dymond J, Gordon LI, Edmond JM, von Herzen RP, Ballard RD, Green K, Williams D, Bainbridge A, Crane K, van Andel TH (1979) Submarine thermal springs on the galápagos rift. Science 203:1073–1083

Couture-Mathieu L, Mathieu JP (1953) Raman spectra of ZnS. Cr Chim 236:371–385

Craddock PR (2009) Geochemical tracers of processes affecting the formation of seafloor hydrothermal fluids and deposits in the Manus Back-arc Basin. Dissertation, Massachusetts Institute of Technology-Woods Hole Oceanographic Institution

Craddock PR, Bach W, Seewald JS, Rouxel OJ, Reeves, Tivey MK (2010)Rare earth element abundances in hydrothermal fluids from the Manus Basin, Papua New Guinea: Indicators of sub-seafloor hydrothermal processes in back-arc basins. Geochim Cosmochim Ac 74:5494–5513

Davies HL, Honza E, Tiffin DL, Lock J, Okuda Y, Keene JB, Murakami F, Kisimoto K (1987) Regional setting and structure of the western Solomon Sea. Geo-Mar Lett 7:153–160

Delaney JR, Mogk DW, Mottl MJ (1987) Quartz-cemented breccias from the Mid-Atlantic Ridge: Samples of a high salinity hydrothermal upflow zone. J Geophys Res 92:9175-9192

Doe BR (1994) Zinc, copper, and lead in mid-ocean ridge basalts and the source rock control on Zn/Pb in ocean-ridge hydrothermal deposits. Geochim Cosmochim Ac 58:2215–2223

Douville E, Bienvenu P, Charlou JL, Donval JP, Fouquet Y, Appriou P, Gamo T (1999) Yttrium and rare earth elements in fluids from various deep-sea hydrothermal systems. Geochim Cosmochim Ac 63(5):627–643

Edmond JM, Measures C, Mangum B, Grant B, Sclater FR, Collier R, Hudson A, Gordon LL, Corliss JB (1979) On the formation of metal-rich deposits at ridge crests. Earth Planet Sc Lett 46:19–30

Fourre E, Jean-Baptiste P, Charlou JL, Donval JP, Ishibashi JI (2006) Helium isotopic composition of hydrothermal fluids from the Manus back-arc Basin, Papua New Guinea. Geochem J 40(3):245–252

Gamo T, Okamura K, Charlou JL, Urabe T, Auzende JM, Ishibashi J, Shitashima K, Chiba H (1997) Acidic and sulfate-rich hydrothermal fluids from the Manus back-arc basin, Papua New Guinea. Geology 25(2):139–142

German CR, Parson LM (1998) Distributions of hydrothermal activity along the Mid-Atlantic Ridge: interplay of magmatic and tectonic controls. Earth Planet Sc Lett 160:327–341

Giacovazzo G, Scordari F, Todisco A, Menchetti S (1976) Crystal structure model for metavoltine from Sierra Gorda. Tscher Miner Petrog 23:155–166

Ginster U, Mottl MJ, Von Herzen RP (1994) Heat flux from black smokers on the Endeavor and Cleft segments, Juan de Fuca Ridge. J Geophys Res 99:4937–4950

Goldfarb MS, Converse DR, Holland HD, Edmond JM (1983) The genesis of hot spring deposits on the East Pacific Rise, 21°N. Econ Geol Monograph 5:184–197

Hannington MD, de Ronde CEJ, Petersen S (2005) Sea-floor tectonics and submarine hydrothermal systems. In: Hedenquist JW, Thompson JFH, Goldfarb RJ, Richards JP (eds.) 100th Anniversary Volume of Economic Geology. Society of Economic Geologists, Littelton, pp 111–141

Harvey PD, Butler IS (1986) Raman spectra of orthorhombic sulfur at 40 K. J Raman Spectrosc 17:329–334

Haymon RM (1983) Growth history of black smoker chimneys. Nature 301:695–698

Haymon RM, Kastner M (1981) Hot spring deposits on the East Pacific Rise at 21 °N" preliminary description of mineralogy and genesis. Earth Planet Sc Lett 53:363–381

Heinrichs H, Schulz-Dobrick B, Wedepohl KH (1980) Terrestrial geochemistry of Cd, Bi, Tl, Pb, Zn, and Rb. Geochim Cosmochim Ac 44:1519–1533

Helgeson HC, Kirkham DH, Flowers GC (1981) Theoretical prediction of the thermodynamic behavior of aqueous electrolytes at high pressures and temperatures. IV. Calculation of activity coefficients, osmotic coefficients, and apparent molal and standard and relative partial molal properties to 600°C and 5 kbar. Am J Sci 281:1249–1517

Herzig PM, Hannington MD, Fouquet Y, von Stackelberg U, Petersen S (1993) Gold-rich polymetallic sulfides from the Lau back arc and implications for the geochemistry of

gold in sea-floor hydrothermal systems of the Southwest Pacific. Econ Geol 88:2182–2209

Humphris SE, Herzig PM, Miller DJ, Alt JC, Becker K, Brown D, Brugmann G, Chiba H, Fouquet Y, Gemmell JB, Guerin G, Hannington MD, Holm NG, Honnorez JJ, Iturrino GJ, Knott R, Ludwig R, Nakamura K, Petersen S, Reysenbach AL, Rona PA, Smith S, Sturz AA, Tivey MK, Zhao X (1995) The internal structure of an active sea-floor massive sulfide deposit. Nature 377(6551):713–716

Kelley DS, Gillis KM, Thompson G (1993) Fluid evolution in submarine magma-hydrothermal systems at the Mid-Atlantic Ridge. J Geophys Res-Sol Ea 98:19579-19596

Kemmitt RDW, Peacock RD (2013) The chemistry of manganese, technetium and rhenium: Pergamon Texts in Inorganic Chemistry Volume 13. Pergamon Press, Oxford Toronto Berlin Sydney Paris Braunschweig 832–833

Klinkhammer GP, Elderfield H, Edmond JM, Mitra A (1994) Geochemical implications of rare earth element patterns in hydrothermal fluids from mid-ocean ridges. Geochim Cosmochim Ac 58(23):5105–5113

Koski RA, Jonasson IR, Kadko DC, Smith VK, Wong FL (1994) Compositions, growth mechanisms, and temporal relations of hydrothermal sulfide-sulfate-silica chimneys at the northern Cleft segment, Juan de Fuca Ridge. J Geophys Res 99B:4813–4832

Libowitzky E, Bechtold A, Friesl P, Oberwandling L, Wildner M (2011) Influence of surface defects on Raman spectra of ore minerals. In: Abstracts, 7th European Conference on Mineralogy and Spectroscopy (ECMS 2011), Potsdam, Germany (http://gfzpublic.gfz-potsdam.de/pubman/item/escidoc:27247)

Lilley MD, Butterfield DA, Olson EJ, Lupton JE, Macko SA, McDuff RE (1993) Anomalous CH_4 and NH_4 concentrations at an unsedimented mid-ocean ridge hydrothermal system. Nature 364:45–47

Lisitsyn AP, Crook K, Bogdanov YA, Zonenshain LP, Murav'yev KG, Tufar W, Gurvich YG, Gordeyev VV, Ivanov GV (1993) A hydrothermal field in the rift zone of the Manus Basin, Bismarck Sea. Int Geol Rev 35(2):105–126

Lutz HD, Müller B (1991) Lattice Vibration Spectra. LXVIII. Single-crystal Raman spectra of marcasite-type iron chalcogenides and pnictides, FeX_2 (X=S, Se, Te; P, As, Sb). Phys Chem Miner 18:265-268

Macdonald, KC, Becker K, Speiss FN, Ballard RD (1980) Hydrothermal heat flux of the "black smoker" vents on the East Pacific Rise. Earth Planet Sc Lett 48:1–7

Martinez F, Taylor B (1996) Backarc spreading, rifting and microplate rotation, between transform faults in the Manus Basin. Mar Geophys Res 18:203–224

Mernagh TP, Trudu AG (1993) A laser Raman microprobe study of some geologically important sulphide minerals. Chem Geol 103:113–127

Mitra A, Elderfield H, Greaves MJ (1994) Rare earth elements in submarine hydrothermal fluids and plumes from the Mid-Atlantic Ridge. Mar Chem 46(3):217–235

Moss R, Scott SD (2001) Geochemistry and mineralogy of gold-rich hydrothermal precipitates from the eastern Manus Basin, Papua New Guinea. Can Mineral 39:957–978

Nasdala L, Witzke T, Ullrich B, Brett R (1998) Gordaite [$Zn_4Na(OH)_6(SO_4)Cl{\cdot}6H_2O$]: second occurrence in the Juan de Fuca Ridge, and new data. American Mineralogist 83:1111–1116

Nasdala L, Smith DC, Kaindl R, Ziemann MA (2004) Raman spectroscopy: analytical perspectives in mineralogical research. In: Beran A, Libowitzky E (eds.): EMU Notes in Mineralogy: Spectroscopic Methods in Mineralogy Vol.6. European Mineralogical Union, pp 281–343

Nielsen SG, Wasylenki LE, Rehkämper M, Peacock CL, Xue Z, Moon EM (2013) Towards an understanding of thallium isotope fractionation during adsorption to manganese oxides. Geochim Cosmochim Ac 117:252–256

Nilsen WG (1969) Raman spectrum of cubic ZnS. Phys Rev 82(3):838–850

Norton D (1984) Theory of hydrothermal systems. Annu Rev Earth Pl Sc 12:155–177

Ohrendorf FW, Haeuseler H (1999) Lattice dynamics of chalcopyrite type compounds. Part I. Vibrational Frequencies. Cryst Res Technol 34(3): 339–349

Pacevski A, Libowitzky E, Zivkovic P, Dimitrijevic R, Cvetkovic L (2008) Copper-bearing pyrite from the Coka Marin polymetallic deposit, Serbia: Mineral inclusions or true solid-solution? Can Mineral 46:249–261

Peacock CL, Moon EM (2012) Oxidative scavenging of thallium by birnessite: explanation for thallium enrichment and stable isotope fractionation in marine ferromanganese precipitates. Geochim Cosmochim Ac 84:297–313

Reeves EP, Seewald JS, Saccocia P, Bach W, Craddock PR, Shanks WC, Sylva SP, Walsh E, Pichler T, Rosner M (2011) Geochemistry of hydrothermal fluids from the PACMANUS, Northeast Pual and Vienna Woods hydrothermal fields, Manus Basin, Papua New Guinea. Geochim Cosmochim Ac 75:1088–1123

Rehkämper M, Nielsen SG (2004) The mass balance of dissolved thallium in the oceans. Mar Chem 85:125–139

Rehkämper M, Frank M, Hein JR, Porcelli D, Halliday A, Ingri J, Liebetrau V (2002) Thallium isotope variations in seawater and hydrogenetic, diagenetic, and hydrothermal ferromanganese deposits. Earth Planet Sc Lett 197:65–81

Saha JK and Podder J (2011) Crystallization of zinc sulphate single crystals and its structural, thermal and optical characterization. J Bangladesh Acad Sci 35(2):203–210

Sandoval SJ, Rivera AL, Irwin JC (2003) Influence of reduced mass differences on the Raman spectra of ternary mixed compounds: $Zn_{1-x}Fe_xS$ and $Zn_{1-x}Mn_xS$. Phys Rev B 68:3031–3039

Schmidt H, Ha NB, Pfannkuche J, Amann H, Kronfeldt HD, Kowalewska G (2004) Detection of PAHs in seawater using surface-enhanced Raman scattering (SERS). Mar Pollut Bull 49:229–234

Seyfried WEJr (1987) Experimental and theoretical constraints on hydrothermal alteration processes at Mid-ocean ridges. Annu Rev Earth Pl Sc 15:317–335

Seyfried WEJr, Ding K (1995) Phase equilibria in subseafloor hydrothermal systems: A review of the role of redox, temperature, pH and dissolved Cl on the chemistry of hot spring fluids at mid-ocean ridges. Geoph Monog Series 91:248–272

Seyfried WEJr, Ding K, Berndt ME, Chen X (1999) Experimental and theoretical controls on the composition of mid-ocean ridge hydrothermal fluids. Rev Econ Geol 8:181–200

Shadlun TN, Bortnikov NS, Bogdanov YuA, Tufar W, Murav'yev KG, Gurvich YeG, Muravitskaya GE, Korina YeA, Topa T (1993) Mineralogy, textures, and formation conditions of modern sulfide ores, Manus Basin rift zone. Int Geol Rev 35(2):127–145

Shanks WC III, Bischoff JL, Rosenbauer RJ (1981) Seawater sulfate reduction and sulfur isotope fractionation in basaltic systems: Interaction of seawater with fayalite and magnetite at 200-350°C. Geochim Cosmochim Ac 45:1977-1995

Shaw AM, Hilton DR, Macpherson CG, Sinton JM (2004) The CO_2–He–Ar–H_2O systematics of the Manus back arc basin: resolving source composition from degassing and contamination effects. Geochim Cosmochim Ac 68(8):1837–1856

Siebert H (1966) Anwendungen der Schwingungsspektroskopie in der anorganische Chemie Anorg. Allg Chem. Einzeldarst. 7, Springer-Verlag, Berlin p 210

Sinton JM, Ford LL, Chappell B, Mcculloch MT (2003) Magma genesis and mantle heterogeneity in the Manus back arc basin, Papua New Guinea. J Petrol 44(1):159–195

Smith DC, Carabatos-Nédelec C (2001) Raman spectroscopy applied to crystals: phenomena and principles, concepts and conventions. In Lewis IR, Edwards HGM (eds.): Handbook of Raman spectroscopy. From the research laboratory to the process line. Pract. Spectrosc. Ser., 28. Marcel Dekker, New York, pp 349–422

Sourisseau C, Cavagnat R, Fouassier M (1991) The vibrational properties and valence force fields of FeS_2, RuS_2 pyrites and FeS_2 marcasite. J Phys Chem Solids 52:537–544

Spiess FN, Macdonald KC, Atwater T, Ballard R, Carranza A, Cordoba D, Cox C, Diaz-Garcia V, Francheteau J, Guerrero J, Hawkins J, Haymon R, Hessler R, Juteau T, Kastner M, Larson R, Luyendyk B, Macdougall D, Miller S, Normark W, Orcutt J, Rangin C (1980) East Pacific Rise: Hot springs and geophysical experiments. Science 207:1421–1433

Spry PG, Gedlinske BL (1987) Tables for determinations of common opaque minerals. Economic Geology Publishing Company, New Haven, pp 52

Taylor B (1979) Bismarck Sea: Evolution of a back-arc basin. Geology 7:171–174

Tivey MA, Bach W, Seewald JS, Tivey MK, Vanko DA, Shipboard Science and Technical Teams (2007) Manus 2006: Hydrothermal systems in the Eastern Manus Basin: Fluid chemistry and magnetic structures as guides to subseafloor processes. Cruise Report R/V Melville, MAGELLAN–06. Woods Hole Oceanographic Institution.

Tivey MK (1995) The influence of hydrothermal fluid composition and advection rates on black smoker chimney mineralogy: Insights from modelling transport and reaction. Geochim Cosmochim Ac 59(10):1933–1949

Tivey MK (2007) Generation of seafloor hydrothermal vent fluids and associated mineral deposits. Oceanography 20(1):50–65

Tivey MK, McDuff RE (1990) Mineral precipitation in the walls of black smoker chimneys: a quantitative model of transport and chemical reactions. J Geophys Res 95(B8):12,617–12,637

Tivey MK, Humphris SE, Thompson G, Hannington MD, Rona PA (1995) Deducing patterns of fluid flow and mixing within the TAG active hydrothermal mound using mineralogical and geochemical data. J Geophys Res-Sol Ea 100(B7):12527–12555

Tufar W (1990a) SONNE 68 - OLGA II research cruise April 29 to June 25, 1990 preliminary cruise report. SOPAC Cruise Report 136:1–9

Tufar W (1990b) Modern Hydrothermal activity, formation of complex massive sulfide deposits and associated vent communities in the Manus Back-Arc Basin (Bismarck Sea, Papua New Guinea). Mitt Osterr Geol Ges 82:183–210

Tufar W (1992) OLGA II – Rezente Komplexmassivsulfiderze (»Schwarze Raucher«) in der Bismarck-See (Papua-Neuguinea). Alma mater philippina, Marburger Universitätsbund e.V., Wintersemester 1992/93, pp 25–33

Von Damm KL (1995) Controls on the chemistry and temporal variability of seafloor hydrothermal fluids. In: Humphris SE, Zierenberg RA, Mullineaux LS, Thomson RE, (eds.), Seafloor hydrothermal systems: Physical, chemical, biological, and geological interactions. AGU Monograph Series No. 91, American Geophysical Union, Washington DC, pp 222–247

Vogt H, Chattopadhyay T, Stalz H (1983) Complete first-order Raman spectra of the pyrite structure compounds FeS_2, MnS_2 and SiP_2. J Phys Chem Solids 44:869–873

White SN (2008) Laser Raman spectroscopy as a technique for identification of seafloor hydrothermal and cold seep minerals. Chem Geol 259:240–252

White SN, Dunk RM, Brewer PG, Peltzer ET, Freeman JJ (2006) In situ Raman analyses of deep-sea hydrothermal and cold seep systems (Gorda Ridge & Hydrate Ridge). Geochem Geophy Geosy 7:Q05023

Yang K, Scott SD (1996) Possible contribution of a metal-rich magmatic fluid to a sea-floor hydrothermal system. Nature 383:420–423

Appendix IV: Curriculum vitae

Personal details

Name	Simon Steger
Nationality	Austrian
E-Mail	simon.st@pgv.at

Education

09/2001 – 06/2009	Gymnasium BG/BRG St. Pölten
06/2009	Graduation, with a scholarly paper on the volcanism of the Canary Islands
Since 10/2010	Studies of Earth Sciences (focus on Mineralogy and Crystallography) at the University of Vienna
07/2013	Short course "Luminescence Spectroscopy and Imaging in Geosciences", Universität Wien. Pre-conference short course in the framework of the CORALS–2013 (Conference on Raman and Luminescence Spectroscopy)
09/2013	Bachelor of Science, Bachelor thesis: “Effekte der Probenpräparation auf Stress in Diamantpulvern – spektroskopische Charakterisierung” (in German). Prof. Lutz Nasdala, thesis advisor

Working experience

07/2007	Employment as Summer intern at Rudolf Leiner Ges.m.b.H., St. Pölten
10/2009 – 06/2010	Civilian service at the nursing home Caritas Haus St. Elisabeth, St. Pölten
10/2013 – 01/2015	Teaching assistant in the BSc course “Introduction to Mineralogy and Crystallography”

Language skills

German	Native language
English	Fluent reading and spoken
Russian	Elementary reading and spoken

Publication

Steger S, Nasdala L, Wagner A (2013) Raman spectra of diamond abrasives and possible artefacts in detecting UHP microdiamond. CORALS–2013, Wien, Austria, July, 2013. Book of abstracts, pp. 95–96